



The Diffraction-Limited Near-Infrared Spectropolarimeter (DL-NIRSP) of the Daniel K. Inouye Solar Telescope (DKIST)

Sarah A. Jaeggli¹ · Haosheng Lin² · Peter Onaka³ · Hubert Yamada³ · Tetsu Anan¹ · Morgan Bonnet³ · Gregory Ching³ · Xiao-Pei Huang⁴ · Maxim Kramar² · Helen McGregor⁵ · Garry Nitta² · Craig Rae³ · Louis Robertson³ · Thomas A. Schad¹ · Paul Toyama³ · Jessica Young³ · Chris Berst⁶ · David M. Harrington¹ · Mary Liang¹ · Myles Puentes⁶ · Predrag Sekulic⁷ · Brett Smith⁸ · Stacey R. Sueoka¹

Received: 14 May 2022 / Accepted: 30 August 2022 / Published online: 20 October 2022
© The Author(s) 2022

Abstract

The *Diffraction-Limited Near-Infrared Spectropolarimeter* (DL-NIRSP) is one of the first-light instruments for the National Science Foundation's *Daniel K. Inouye Solar Telescope* (DKIST). DL-NIRSP is an integral-field, dual-beam spectropolarimeter intended for studying magnetically sensitive spectral lines in the Sun's photosphere, chromosphere, and corona with high spectral resolution and polarimetric accuracy. Two novel fiber-optic integral-field units (IFUs), paired with selectable feed optics and a field-scanning mirror provide great flexibility in spatial sampling (0.03", 0.08", and 0.5") and field coverage (2' × 2'). The IFUs allow DL-NIRSP to record all the spectra from a 2D field of view simultaneously, enabling the instrument to study the evolution of highly dynamic events. The spectrograph is an all-reflecting, near-Littrow design, which achieves a resolving power of approximately 125,000. Multiple wavelengths can be observed simultaneously using three spectral arms: one for visible wavelengths (500–900 nm) and two for infrared wavelengths (900–1350 nm and 1350–1800 nm). Each supporting camera sub-system is capable of a 30-Hz frame rate, making it possible to track dynamic phenomena on the Sun.

Keywords Instrumentation and data management

Contents

1 Introduction	2
2 Scientific Objectives and Design Concept	4
3 Elements of DL-NIRSP	5
3.1 Feed Optics	7
3.2 Spectrograph	10
3.3 BiFOIS	15

This article belongs to the Topical Collection:
The Daniel K. Inouye Solar Telescope (DKIST)
Guest Editors: Thomas R. Rimmele, Philip R. Goode, Michael Knölker, Jeffrey R. Kuhn, and Robert Rosner

Extended author information available on the last page of the article

3.4 Detectors	17
3.5 Polarization System	18
3.6 Software	19
4 Optical Alignment	21
4.1 Feed-Optics Alignment	22
4.2 Spectrograph Alignment	22
5 As-Built Performance	25
5.1 Spatial Resolution	25
5.2 Spectral Resolution	26
5.3 Wavelength Coverage and Throughput	27
5.4 Polarization	28
5.5 Stability	29
5.6 Spectrograph Configurations	31
6 First Results	32
6.1 A Pore in the Photosphere	32
6.2 Active-Region Corona	33
7 Conclusions and Outlook	35
Acknowledgments	37
References	38
Authors and Affiliations	42

1. Introduction

The *Diffraction-Limited Near-Infrared Spectropolarimeter* (DL-NIRSP) is one of the first-light instruments of the *Daniel K. Inouye Solar Telescope* (DKIST; Rimmele et al., 2020), developed at the Institute for Astronomy (IfA) of the University of Hawai'i (UH). DKIST is the National Science Foundation's (NSF) new flagship solar telescope to support the solar-physics research effort of the US and the broader worldwide solar communities for the 21st century.

DKIST was designed from the ground up as a general-purpose facility that can be used for research of a broad range of science topics, ranging from the generation of solar magnetism to the physics of energetic solar eruptions (Rast et al., 2021). It is a 4-m aperture, off-axis Gregorian telescope equipped with a high-order adaptive optics system (HOAO; Rimmele et al., 2006; Richards et al., 2010; Johnson et al., 2018) to enable high spatial observations of the Sun at the spatial scale of fundamental plasma processes. DKIST is designed for high-precision polarimetry (Harrington et al., 2022) and is also a coronagraphic telescope, with a superpolished primary mirror, a Lyot stop, and a limb occulter to facilitate observations of the faint solar corona at small elongations from the bright solar disk.

DKIST is equipped with five facility-class instruments, each with unique capabilities and priority science objectives. The DKIST optical path allows for multiple instruments to be run in parallel to address diverse use cases. In addition to DL-NIRSP, these instruments include the *Visible Broadband Imager* (VBI; Wöger et al., 2021), the *Visible Spectropolarimeter* (ViSP; de Wijn et al., 2022), the *Cryogenic Near-Infrared Spectropolarimeter* (CryoNIRSP; Fehlmann, 2022), and the *Visible Tunable Filter* (VTF; von der Lühe et al., 2022). A unique feature of DL-NIRSP that is not available in the other facility instruments is its capability to perform integral-field spectroscopy (IFS), or the simultaneous observation of the spectra from a spatially resolved 2D field of view. One of the primary science goals of DL-NIRSP is the study of the interaction between the magnetic fields and the plasma of the dynamic solar

atmosphere. As the evolutionary timescales of solar magnetism range from hours, for large-scale structures like sunspots or filaments, to minutes, for solar granules, to seconds during energetic eruptions, it is critical that DL-NIRSP is equipped with the ability to observe a 2D field of view with high temporal resolution sufficient to resolve the dynamic timescales of these energetic events.

Dynamic events that cause the exchange of magnetic energy and heating through different layers of the solar atmosphere, e.g. solar flares, filament eruptions, and coronal mass ejections (CMEs), demand an instrument capable of simultaneous observations of the polarized spectra of multiple spectral lines from a 3D volume of the solar atmosphere with very high spatial, spectral, and temporal resolution. For observations on the solar disk, this requires simultaneous observations of spectral lines originating from the photospheric and chromospheric levels. For the study of coronal magnetism, this requires simultaneous coverage of coronal emission lines with ionization temperatures spanning a large range. This capability is critical for understanding the physics of energetic solar eruptions that drive space weather.

These requirements are the primary drivers that have guided the design of DL-NIRSP. In particular, the high temporal resolution requirement has led to the decision to use fiber-optic integral field units (IFUs) to achieve fast temporal coverage along with simultaneous 2D field coverage.

Multi-object spectrographs, integral-field units, and integral-field spectrographs have a long history in nighttime astronomical research (Ramsay Howat et al., 2004; Smeed et al., 2013; Henault et al., 2003); however, their application for solar observations did not start until the early 2000s (Lin, Kuhn, and Coulter, 2004; Lin, 2012; Ren, Keller, and Plymate, 2009). While the principles and technologies for IFS were well developed, solar spectroscopic observations, especially those related to magnetic-field diagnostics, require observation of polarized spectra at very high spectral resolution ($R \geq 100,000$) over a narrow spectral window ($\lambda/\Delta\lambda \approx 1000$) around the spectral lines. Conventional IFUs built with large-core multi-mode fibers or polished-glass image slicers are difficult to optimize for solar observations. For example, the *GREGOR Infrared Spectrograph* (GRIS: Collados et al., 2012) is equipped with a polished-glass image slicer with a 100- μm slit width, which requires a large spectrograph to achieve high spectral resolution.

The development of multi-slit spectrographs, such as the photographic system of Martin et al. (1974) and the *Facility Infrared Spectropolarimeter* (Jaeggli et al., 2010), laid the groundwork for integral-field spectroscopy with DL-NIRSP. The multi-slit approach allows for efficient use of modern large-format detectors. High spectral resolution can be achieved over very narrow spectral bandpasses by using high-performance narrow-band filters to keep spectra from different slits and orders of the spectrograph from overlapping on the detector. Multi-slit spectrographs allow for more rapid scanning of large fields of view than traditional long-slit spectrographs, and the development of instruments with multi-slit capability continues to grow (Lin, 2016; Schad and Lin, 2017; De Pontieu et al., 2020).

A new *Birefringent Fiber-Optic Image Slicer* (BiFOIS: Lin and Versteegh, 2006; Schad et al., 2014) was developed to address the special needs of solar integral-field spectropolarimetry. BiFOIS takes advantage of the multi-slit approach by taking a small integral field at the focal plane and coherently mapping to multiple linear arrays that form the spectrograph entrance slits using fiber-optic ribbons. DL-NIRSP is equipped with two BiFOIS IFUs (BiFOIS-36 and BiFOIS-72) optimized for high spatial resolution and wide-field coverage, respectively. These two IFUs, combined with a flexible-feed optical system and scanning mirror, enable DL-NIRSP to observe in three spatial resolution modes to help address diverse science objectives.

This article documents the details of the optical system as well as the designed performance parameters. Examples of laboratory-performance evaluation results of the critical optical components and sub-systems will also be described. First, we provide the scientific motivation for the design of the instrument in Section 2. We discuss the essential components of the instrument in Section 3, including the optical, polarimetric, and software systems. We provide a description of the techniques and procedure used for the optical alignment of the instrument in Section 4. In Section 5 we present some of the critical as-built instrument-performance measurements. In Section 6 we present the first observations from DL-NIRSP on the solar disk and in the corona. In Section 7 we summarize our work and discuss some future developments for DL-NIRSP.

2. Scientific Objectives and Design Concept

DL-NIRSP was developed to target specific needs in order to address some of the major scientific questions in solar physics. How is the magnetic field generated and recycled by the Sun's global and small-scale dynamos (Cameron, Dikpati, and Brandenburg, 2017; Borrero et al., 2017)? How are the chromosphere and corona heated to high temperatures (De Moortel and Browning, 2015; Klimchuk, 2015)? How is the solar wind accelerated (Cramer and Winebarger, 2019)? What triggers solar flares, coronal mass ejections, and other eruptive phenomena on the Sun that impact space weather (Benz, 2017; Green et al., 2018)? In order to provide new insight into these questions, the design of DL-NIRSP was driven by five major factors:

- The need for high spatial resolution observations.
- The need for sensitive spectropolarimetry.
- The need for high-cadence observations.
- The need for multi-wavelength observations.
- The need for coronal spectropolarimetry.

In the following paragraphs we briefly discuss some example science cases and the instrument parameters necessary to meet these needs.

One of the strongest cases for diffraction-limited integral-field spectropolarimetry comes from a need to study the smallest magnetic elements that can be seen on the Sun. Compact magnetic elements with ≈ 1 kG magnetic-field strength are ubiquitous in the quiet-Sun photosphere where they appear in the downflow lanes of solar granulation. These elements are largely unresolved in current spectropolarimetric measurements (Lagg et al., 2010), but they display systematic features in their intensity, velocity, and dynamical behavior, in addition to the magnetic field, that set them apart from regions with weaker apparent magnetic fields. Recent observations with DKIST/VBI have revealed the detailed structure and dynamics occurring within bright features that correspond to these magnetic elements (Wöger et al., 2021). High spatial resolution magnetohydrodynamic simulations of the solar convection zone and photosphere indicate that 50% of the magnetic energy in the quiet Sun may exist on scales of smaller than 100 km (Rempel, 2014), and therefore understanding these small-scale features might be important for understanding the Sun's magnetic-energy budget. Use of an integral field with spatial resolution limited only by the diffraction of DKIST allows one to continuously track the evolution of compact solar features within a small field of view.

Sensitive observations are necessary to make headway on problems involving magnetic waves in the solar atmosphere, e.g. magnetoacoustic waves, transverse/torsional Alfvén waves, and kink waves. The magnetic-field variation produced by these phenomena is small,

at about the 10-G level as seen in photospheric spectral lines (Fujimura and Tsuneta, 2009). Given that the spectral lines themselves are not fully polarized, a polarization sensitivity of at least 10^{-4} with respect to the continuum intensity level is required to see these changes in the magnetic field in the chromosphere (Quintero Noda et al., 2017). The observations must also be taken with a cadence sufficient to fully sample the three- or five-minute oscillation period common to the photosphere and chromosphere.

There are many problems in solar physics where simultaneous multi-wavelength observations are necessary. Using multi-wavelength observations, it is possible to combine diagnostics sensitive to different plasma properties and target different heights in the solar atmosphere, building up a three-dimensional picture. Co-temporal and co-spatial measurements of magnetic-field diagnostics formed at different heights can reveal the propagation of magnetic waves (Felipe et al., 2010), the morphology of magnetic-flux tubes (Morosin et al., 2020), and the spatial and temporal distributions of the electric-current vector (Anan et al., 2021). Multi-height magnetic-field information is also critical for informing and validating magnetic-field extrapolations based on photospheric observations (Metcalfe et al., 1995; Kawabata et al., 2020), which are heavily relied on for coronal studies.

Ground-based spectral observations of the off-limb solar corona offer many advantages for studying its energization and dynamics, especially as it pertains to solar-wind acceleration and coronal mass ejections (Landi, Habbal, and Tomczyk, 2016). The key benefit provided by diagnostics at visible and infrared wavelengths lies in their ability to remotely probe the magnetic field in the corona via polarization, as reviewed by Casini, White, and Judge (2017). Lin, Penn, and Tomczyk (2000) first observed circular polarization from a coronal emission line, which results from the longitudinal component of the Zeeman effect. Together with resonance-scattered polarization, constraints on the line-of-sight component and the orientation on the plane of sky of the magnetic field bolsters vector-tomographic efforts for reconstructing the 3D coronal magnetic field (Kramar, Inhester, and Solanki, 2006; Kramar et al., 2013). To take full advantage of such diagnostics, simultaneous multi-wavelength observations are necessary to address the intertwined thermal and magnetic-field effects on the spectra, as discussed, e.g. by Dima and Schad (2020) and Schad and Dima (2020).

A single instrument cannot simultaneously achieve high cadence with high spatial resolution and high signal to noise over a large field of view at all wavelengths. There must be a trade-off between these parameters. By building DL-NIRSP as a multi-wavelength integral-field spectropolarimeter with field-scanning capability and different spatial-resolution modes, a high-resolution mode for diffraction-limited observations, a mid-resolution mode for cases requiring high signal to noise or cadence, and a wide-field mode for coronal observations, the end user is given the ability to select the trade-offs that allow them to address their science use cases most effectively using set combinations of sensitive magnetic-field diagnostic spectral lines. The requirements for DL-NIRSP, driven by these science motivators, are given in Table 1. The wavelengths of DL-NIRSP were selected to sample diagnostics from a diverse range of heights, temperatures, and magnetic-field regimes in the solar atmosphere. These wavelengths are listed in Table 2 along with the diagnostic species and their potential uses. Rescoping, rebudgeting, and the realities of implementation have changed the instrument slightly from its original design over the course of the construction project.

3. Elements of DL-NIRSP

DL-NIRSP is composed of two major optical systems: the feed optics and the spectrograph. In the following sub-sections we discuss the elements and the layout of these two optical

Table 1 DL-NIRSP High-Level Design Specifications.

Science Requirement	Goal	As-Built
Spectral Coverage	900–2500 nm	500–1800 nm
Spectral Resolving Power	50,000–200,000	> 105,000
Spatial Sampling	$1.22\lambda/2D$ @ 900 nm	TBD
Spatial Field of View	2.8' round, 2' square	Same
True Imaging Spectropolarimeter	IFU with 2048 spatial sampling elements	IFU with 3840 spatial sampling elements
Polarimetric Accuracy	5×10^{-4}	TBD
Modulation Cadence	0.1 sec.	0.3 sec.
Modulation Efficiency	> 0.1	> 0.4
Multi-wavelength	3 Simultaneous Channels	Same
Simultaneous Operation	AO corrected with VBI, ViSP, VTF	AO corrected with VBI, ViSP, VTF; also with CryoNIRSP ^a

^aAfter FIDO beam-splitter upgrade. CryoNIRSP is not corrected by the high-order adaptive-optics system.

Table 2 Current DL-NIRSP Wavelengths.

Arm	Wavelength [nm]	Diagnostic Species	Uses
1	530.3	[Fe XIV]	Coronal magnetic fields, $\log(T_{\max} [\text{K}]) = 6.3^a$
1	587.6	He I D3	Chromosphere, Filament magnetic fields
1	630.2	Fe I	Photospheric magnetic fields
1	789.2	[Fe XI]	Coronal magnetic fields, $\log(T_{\max} [\text{K}]) = 6.2$
1	854.2	Ca II	Chromospheric magnetic fields
2	1074.7	[Fe XIII]	Coronal magnetic fields, density, $\log(T_{\max} [\text{K}]) = 6.3$
2	1079.8	[Fe XIII]	Coronal magnetic fields, density, $\log(T_{\max} [\text{K}]) = 6.3$
2	1083.0	He I, Si I	Photospheric and chromospheric magnetic fields
3	1430.0	[Si X]	Coronal magnetic fields, $\log(T_{\max} [\text{K}]) = 6.2$
3	1565.0	Fe I, OH	Photospheric magnetic fields, cool photosphere

^aThe coronal emission-line temperatures [T_{\max}] come from the CHIANTI atomic-database line list (Dere et al., 1997; Del Zanna et al., 2021).

systems, as well as critical components that make DL-NIRSP a functional imaging spectropolarimeter. Figure 1 shows a rendering of the DL-NIRSP instrument in the context of the coude laboratory with the full light path from DKIST M7 through the DL-NIRSP spectrograph. Figure 2 shows a panoramic overview of the real DL-NIRSP components in the coude lab as they are currently installed.

The DKIST optical beam in the coude lab is horizontally oriented and is nearly collimated after DKIST M8. Following the reflection from the wavefront-correction (WFC) system deformable mirror (DKIST M10), the beam encounters the *Facility Instrument Distribution Optics* (FIDO; Harrington et al., 2021) which is an interchangeable series of windows and long-pass dichroic beam-splitters used to provide different instruments with light from various portions of the optical and infrared spectrum. The light traveling to DL-NIRSP follows the transmitted path through the coude locations (CL) for the FIDO beam-splitters:

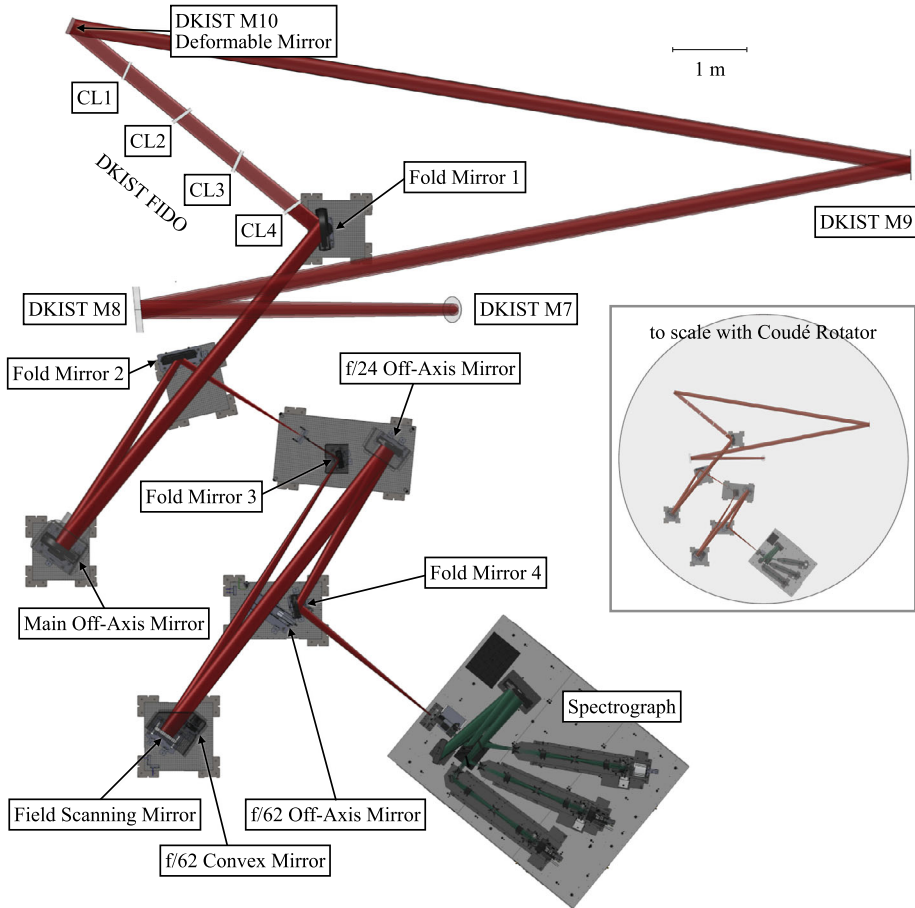


Figure 1 A rendering of the instrument hardware and optical train from DKIST M7 through the DL-NIRSP spectrograph. The feed optics are shown in the $f/24$ configuration.

CL1 (reflects to WFC), CL2 (reflects to ViSP), CL3 (reflects to VBI Red and VTF), and CL4 (reflects to an unused path). During coordinated observations, DL-NIRSP may receive part or none of the visible spectrum, but infrared wavelengths longer than $1 \mu\text{m}$ are always available to DL-NIRSP unless CryoNIRSP is observing, as it currently receives the full optical beam using a fold mirror placed between M9 and M10 (not shown in Figure 1). An upgrade of the current M9a mirror to a beam-splitter will make observations between CryoNIRSP and other instruments possible.

3.1. Feed Optics

The DL-NIRSP feed optics re-image the light within the $2.8'$ field of view of DKIST at different plate scales to provide different spatial-sampling modes. The feed optics also incorporate a scanning mechanism for observing fields of view larger than what is accommodated instantaneously by the IFU, up to $2.8'$. The feed optics were designed as an all-reflecting optical train, making use of the protected silver coatings used elsewhere in DKIST (Harring-

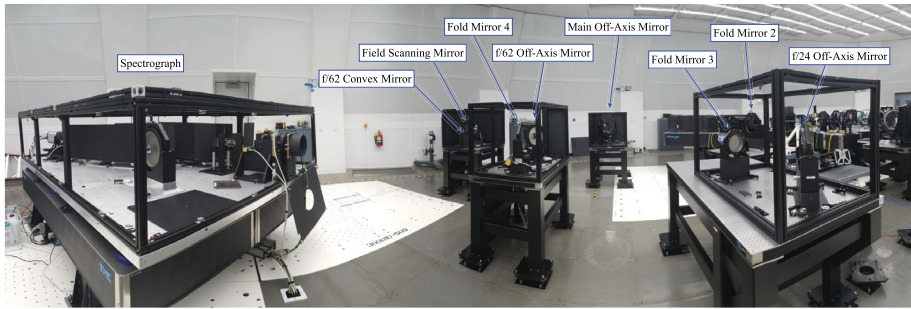


Figure 2 A panoramic view, taken on 23 November 2021, of the DL-NIRSP spectrograph (*left*) and feed optics (*center*, *right*) in the DKIST coude laboratory. The enclosure covers for control of scattered light have been removed so that the optical components can be seen.

Table 3 Feed-Optics Elements.

Name	Diameter [mm]	Radius of Curvature [mm]	Conic Constant	Offaxis Distance [mm]
Fold Mirror 1	380	∞		
Main Off-axis Mirror	400	-9600.000	-1.376	600
Fold Mirror 2	300	∞		
Fold Mirror 3	150	∞		
Field Scanning Mirror	220	-9600.000	0.000	0
f/24 Off-axis Mirror	250	-9600.000	-0.640	918
f/62 Off-axis Mirror	230	-5855.785	-0.252	481
f/62 Convex Mirror	100	2852.493	2.832	0
Fold Mirror 4	203	∞		

ton, Sueoka, and White, 2019) to provide excellent throughput as a function of wavelength as well as achromatic imaging performance. Several of the powered (i.e. with curvature) mirrors are off-axis conic sections. The shape and configuration of these mirrors were designed to compensate for wavefront distortion introduced in the optical path of the telescope and help the feed optics achieve diffraction-limited performance. The optical parameters for each mirror are given in Table 3, and an optical ray trace of the DL-NIRSP feed optics is shown in Figure 3.

The DL-NIRSP fold mirror 1 (Feed FM-1) directs the nearly collimated light from FIDO to the main off-axis mirror (Feed OAM), a concave hyperboloid, which begins to focus the light. This converging beam encounters fold mirror 2 (Feed FM-2) and then comes to the intermediate focus, which is approximately $f/24$. This focus is not optimized for wavefront error and has a significant astigmatism. The focused beam then begins to diverge as it encounters fold mirror 3 (Feed FM-3), which directs it to the field-scanning mirror (FSM). The DKIST intermediate pupil image incident on M10 (the deformable mirror) is re-imaged here with unit magnification. The FSM is a spherical mirror mounted in a piezo-driven tip/tilt mount that can adjust the centering of the field of view at the final focal plane of the feed optics. The motion of this mount is controlled at the $0.3\text{-}\mu\text{rad}$ level, equivalent to $0.006''$ on the sky.

After the FSM, the beam is once again nearly collimated, and the optical path has two possible configurations that can be swapped by moving mirrors on motorized stages. The

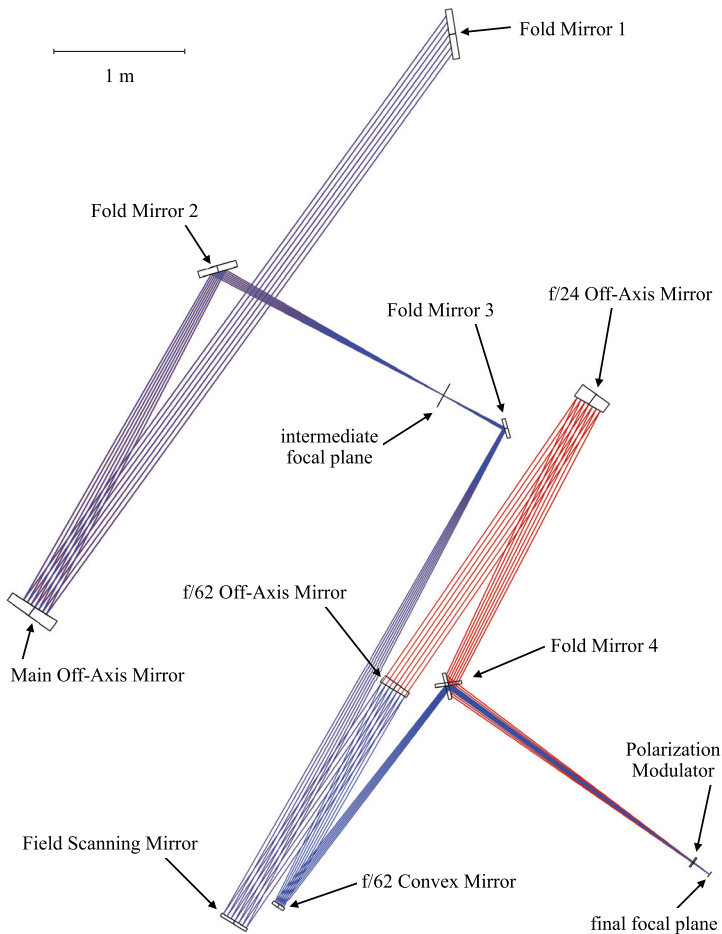


Figure 3 Ray trace of the two main optical paths through the feed optics starting from DL-NIRSP Fold Mirror 1. The *blue trace* shows $f/62$ High-Res mode and the *red trace* shows $f/24$ Mid-Res mode. The $f/8$ Wide-Field mode (not shown) modifies the $f/24$ optical path by inserting the coronal lens immediately before the IFU, but it is otherwise identical.

first configuration provides the Mid-Res mode with an $f/24$ focal ratio and the Wide-Field (coronal) mode with an $f/8$ focal ratio; it is shown by the red ray trace in Figure 3. In this case, the light proceeds from the FSM to the $f/24$ mirror (Feed MF24), an off-axis prolate ellipsoid. The light begins to converge and then reflects from fold mirror 4 (Feed FM-4): a flat mirror on a motorized rotation stage. Feed FM-4 directs the light to the final focal plane at the spectrograph. Either BiFOIS-36 or BiFOIS-72 with the coronal lens may be used with this configuration to provide the spatial sampling for the Mid-Res or Wide-Field modes, respectively. The coronal lens changes the native $f/24$ beam to $f/8$, providing greater field-of-view coverage.

The second feed-optics configuration provides the diffraction-limited High-Res mode with an $f/62$ focal ratio and may only be used with BiFOIS-36; it is shown by the blue ray trace in Figure 3. In this instance, the collimated light from the FSM is intercepted by the $f/62$ off-axis mirror (Feed MF62-1), another prolate ellipsoid. This mirror sits on a linear stage

Table 4 Spectrograph Optical Elements.

Name	Physical Dimensions	Parameters
Heat Stop	30-mm diameter aperture	Actively cooled copper aperture plate
Polarization Modulator	38-mm diameter	Index-matched Polycarbonate with BK-7 windows
f/8 Coronal Lens	36 mm	Triplet demagnifying lens
IFU-36	150 mm long	36 μm imaging pixel
IFU-72	150 mm long	72 μm imaging pixel
Fold Mirror 1	116 \times 74 mm	Flat Mirror
Offaxis Mirror	350-mm diameter	Radius of Curvature:-2500 mm, Conic Constant: -1.123, Offaxis Distance: 260 mm
Diffraction Grating	300 \times 150 mm	Grating Constant: 23.2 mm^{-1} , Blaze Angle: 63°
Beam-Splitter 1	160 \times 86 mm	Dichroic 950 nm long pass
Beam-Splitter 2	140 \times 64 mm	Dichroic 1350 nm long pass
Fold Mirror 2	92 \times 64 mm	Flat Mirror
Collimator Lens	92-mm diameter	Triplet, Front Focal Length: 334.3 mm
Wollaston Prism	50 \times 50 mm	Quartz Crystal, 34° internal wedge angle
Camera Lens	92-mm diameter	Triplet, Back Focal Length: 334.3 mm
Narrow-band Filter	70-mm diameter	Narrow-band and Bandpass filter coating

capable of moving the mirror in and out of the optical path. The converging beam is then modified by a convex mirror (Feed MF62-2), an on-axis oblate ellipsoid, which makes the beam convergence more gentle, providing the $f/62$ final focal ratio. Together, Feed MF62-1 and MF62-2 form a variant of a Dall–Kirkham telescope configuration. Feed FM-4 is rotated with respect to its $f/24$ position so that the $f/62$ beam reflects from it and comes to a final focus at the spectrograph.

3.2. Spectrograph

The DL-NIRSP spectrograph optics are responsible for carrying out all of the spatial, spectral, and polarimetric light analysis necessary for making observations. A rendering of the spectrograph is shown in Figure 4 with all of the major components labeled, and the relevant parameters for each optic are given in Table 4. A top-down view of the optical ray trace in Figure 5 shows the location of focal planes more clearly. The optics of the spectrograph are mounted on the *Instrument Support Platform* (ISP), which is an air-bearing platform capable of lifting the full weight of the spectrograph and positioning it with μm precision with a range of several centimeters in each direction. The ISP is designed to allow a precision final positional and angular alignment of the spectrograph as a whole to the incoming beam from the feed-optics system. The ISP rests on top of two flat-topped optical tables that have been joined together, and these are each mounted to the coude rotator platform. When the ISP is deactivated after the final alignment, it is rigidly bolted to the lower optical tables, although it is still resting on the air-bearing pucks (the blue disks in Figure 4).

The feed optics produce a focused image on the IFU, but there are a few components upstream of the IFU that are important for the function of the spectrograph. A heat stop (not included in Figure 4 but visible in Figure 2) with a cylindrical baffle is mounted on the front edge of the ISP nearest to the feed optics. The heat stop is an actively cooled aperture stop that transmits an unvignetted field of view to the polarization modulator and

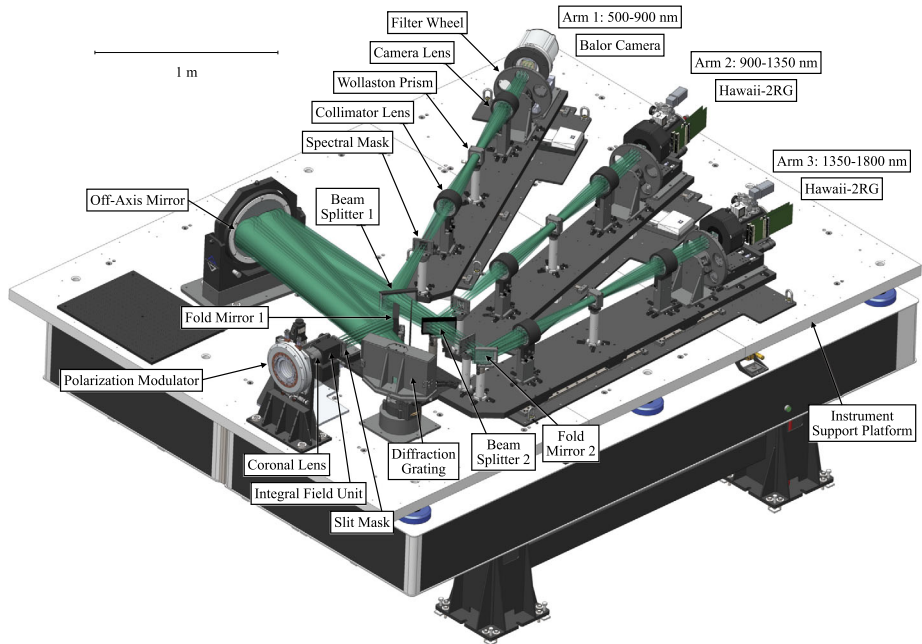


Figure 4 A rendering of the DL-NIRSP spectrograph with the essential optical components labeled. Spectrograph Arms 1, 2, and 3 have similar optical trains; only the components on Arm 1 are labeled for simplicity. The enclosure and covers are not shown, but the spectrograph optics are fully enclosed on the top and sides to control scattered light.

IFU, and collects the unused beam overflow from the 2.8' FOV of DKIST. This prevents excess heating of the instrument hardware and mitigates scattering of the solar beam into the spectrograph. The polarization modulator in its rotation mount sits immediately behind the heat stop. This component will be discussed further in the context of the polarization system in Section 3.5.

The IFU assembly sits behind the polarization modulator on the front end of the ISP. The two BiFOIS IFUs with image sampling pixels of 36 and 72 μm are mounted together on a motorized elevator stage that translates vertically to select the resolution mode in combination with the feed-optics configuration. The lens that provides the f/8 Wide-Field mode for coronal studies is also mounted on this stage immediately in front of BiFOIS-72.¹ The IFU takes a rectangular area of the input image and reformats it into an array of four vertical slits that form the input to the spectrograph. Due to the off-axis design of the spectrograph, the plane formed by the exit slits of the IFU is tilted at a 3.394° angle with respect to the propagation direction of the beam. If this were not the case, the spectrograph would have a tilted image plane at the final focus, requiring each camera to be tilted at the same angle. The design and properties of the BiFOIS IFUs are discussed in more detail in Section 3.3. The final part of the IFU assembly is a motorized mask that sits immediately behind the IFU slits. This mask has apertures with variable spacing that make it possible to illuminate the spec-

¹As of this writing, BiFOIS-72 and the coronal lens have not been integrated and aligned. All performance testing is based on BiFOIS-36.

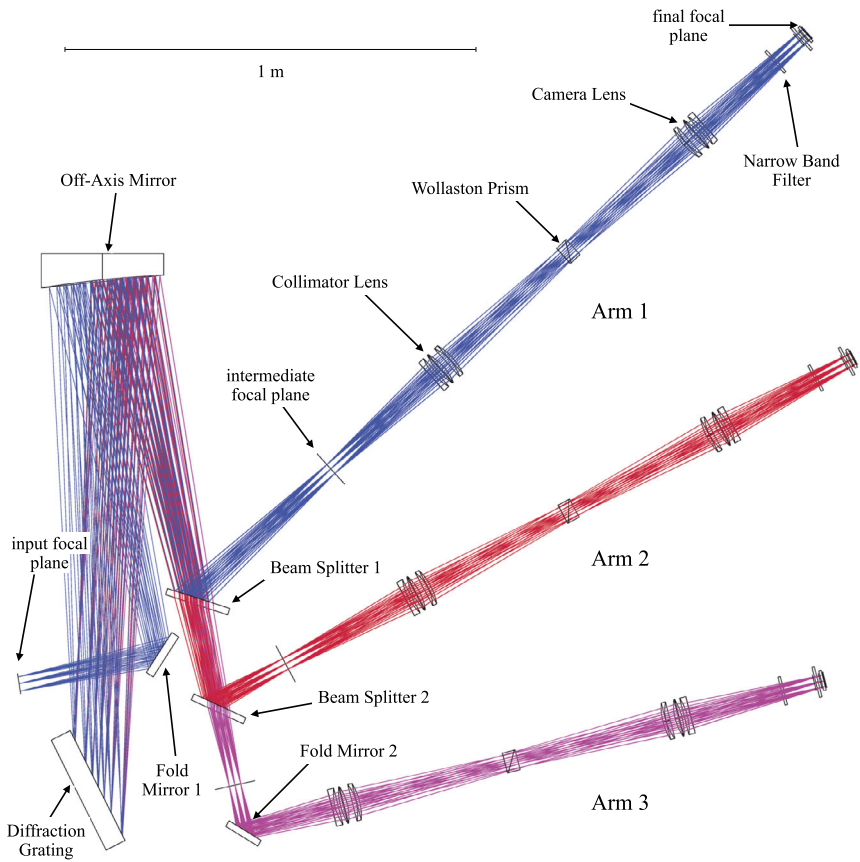


Figure 5 Ray trace of the optical path through the spectrograph for 630 (blue), 1083 (red), and 1565 nm (magenta). The grating and arm positions shown have been optimized to achieve the best wavefront error for each wavelength.

trograph with all slits, block all slits, or allow individual slits to illuminate the spectrograph for calibration purposes.

The front end of the DL-NIRSP spectrograph was designed as an all-reflecting, off-axis Littrow spectrograph to provide good instrument efficiency and achromatic behavior over a range of visible and infrared wavelengths. The light emerging from the fiber-optic IFU is telecentric with a nominal $f/12$ Gaussian beam profile, and the spectrograph optics are matched to this focal ratio. A flat mirror (Spectrograph FM-1) folds the light from the IFU exit slits toward the left side (from the views shown in Figures 4 and 5) of an off-axis hyperboloid mirror (Spectrograph OAM). The diverging beam is collimated and reflected toward the diffraction grating located one focal length (≈ 1250 mm) away, where the light is spectrally dispersed. This grating has a coarse groove density of 23.2 mm^{-1} and a steep blaze angle of 63° that allow DL-NIRSP to achieve high dispersion at visible and infrared wavelengths while still achieving good efficiency. The dispersed light from the grating travels back to the right side (from the views shown in Figures 4 and 5) of the Spectrograph OAM and begins to refocus. This spectrograph design preserves the telecentric-beam configuration of the beam exiting from the IFU slits.

In the converging beam leaving the OAM, DL-NIRSP has two dichroic beam-splitters, which serve a similar purpose as the DKIST FIDO optics. This set of optics allows the visible and infrared light to be distributed to the three different cameras. The converging beam from the Spectrograph OAM first encounters a dichroic beam-splitter (Spectrograph BS-1), which reflects visible light shorter than 900 nm to Arm 1. The wavelengths longer than 900 nm are transmitted through BS-1 to a second dichroic beam-splitter (Spectrograph BS-2), which reflects wavelengths shorter than 1350 nm to Arm 2. Wavelengths longer than 1350 nm continue to the Arm 3 optics. The performance of these beam-splitters has been rigorously characterized by the DKIST polarization team and can be found in Harrington et al. (2021).

The components for each spectral arm of DL-NIRSP are nearly identical, except for wavelength-specific coatings. To make clear the purpose of the optical components of the spectral arm, we discuss the manner in which they can be considered to operate on the spectrum, rather than their order in the light path. The converging beam from the Spectrograph OAM is reflected or transmitted by the beam-splitters and comes to an intermediate focus at the front end of each spectral arm. The light from the intermediate focus is re-imaged 1:1 by a pair of achromatic lenses (the collimator and camera lenses in Figures 4 and 5) and focused on the camera detector. The visible and infrared detectors are discussed further in Section 3.4.

A narrow-band bandpass isolation filter ($\lambda/\Delta\lambda \approx 750$) sits in the telecentric converging beam just in front of the detector to enable the multi-slit design of the spectrograph. This filter has both broad- and narrow-band coatings so it can select the spectral region of interest around the diagnostics listed in Table 2 and reject light from nearby spectral orders that are also transmitted by the spectrograph optical path. Although the filter spectral profiles are extremely narrow and have steep shoulders, their demanding design specifications are relaxed by up to a factor of two in bandwidth in comparison to the bandpass that the instrument achieves through the use of a spectral mask in the intermediate focus at the front end of the spectral arm. The spectral mask is a field stop with four slots with width and spacing that have been tailored to the re-imaged IFU slit spacing for that arm. The spectral mask creates a large, dark gap between each spectrum from the IFU slits, so that each spectrum can be dispersed horizontally by the Wollaston prism, which sits at the pupil plane in the middle of the lens relay. The narrow-band filter and the spectral mask create an effective spectral bandwidth coverage of $\lambda/\Delta\lambda \approx 1250$. The Wollaston prism splits each individual image into two images with an orthogonal linear polarization direction. Figure 6 shows an example of the 630-nm spectra from Arm 1 produced by this complex stack-up of optical elements, which efficiently fills the detector area.

The DL-NIRSP spectrograph is not static; it must be reconfigured to observe different combinations of wavelengths with the three spectral arms. The spectrograph is designed around a nominal angle of 5° between the incident and outgoing rays (i.e. $\alpha - \beta$ as in Equations 2–6 of Palmer, 2020); this angle is sometimes called the Littrow angle. As the blaze orders for different wavelengths do not necessarily overlap the same optical path, the light-distribution optics following the spectrograph need to be capable of accepting a range of Littrow angles, and each spectral arm must be able to move to center the bandpass on the camera. The optics for each spectral arm, from the spectral mask up to and including the camera, are all mounted together on a large translation stage, indicated by the black raised platforms in Figure 4. It is necessary to rotate the spectrograph grating and translate the spectral arms to observe different combinations of wavelengths together, but because the optical path through the instrument must change, it is not always possible to achieve the highest image quality with all of the spectral arms at once. For simultaneous wavelength

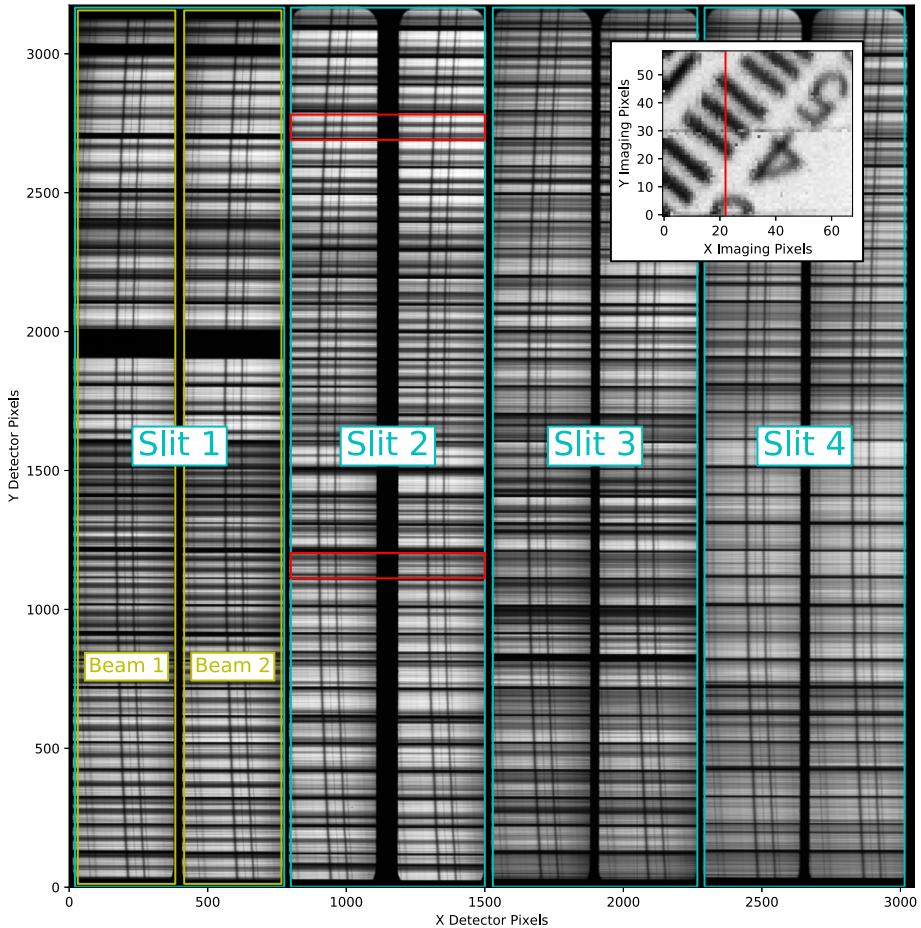


Figure 6 A raw image from Arm 1 of DL-NIRSP configured for 630 nm showing the essential behavior of the IFU-36 with the spectrograph. During this exposure, DKIST was illuminated with sunlight with a resolution target in place and re-imaged by the DL-NIRSP Mid-Res optics on the IFU entrance. The inset image shows the spatially reconstructed image from the IFU with the flat field applied. The *red rectangles* in the raw image indicate the spectra corresponding to the region covered by the *red line* in the reconstructed image.

combinations, the different wavelengths traverse different optical paths through the instrument, in particular they fall on different portions of the off-axis mirror after returning from the grating. This behavior can be seen in Figure 5 as a slight separation of the red, blue, and magenta optical ray traces. The “misalignment” from the best optical path introduces wavefront error, which degrades the image. The current grating, with a groove density of 23.2 mm^{-1} and a 63° blaze angle, cannot provide high diffraction efficiency simultaneously for all combinations of the current wavelengths available for DL-NIRSP (see Section 5.6) and may limit future wavelength upgrades. An additional grating, for example, one with a groove density of 31.6 mm^{-1} and a 63° blaze angle, would allow the user to optimize the image quality and diffraction efficiency for a larger number of three-wavelength combinations.

3.3. BiFOIS

DL-NIRSP has two fiber-optic image slicers, BiFOIS-36 and BiFOIS-72, which are each composed of a fiber-optic bundle that transfers the light from a densely packed rectangular array on the front surface to four linear arrays on the back surface of the device. Following the work of Lin and Versteegh (2006) and Schad et al. (2014), the first BiFOIS was installed in an experimental instrument (Lin, 2012) at the *Dunn Solar Telescope*, and its scientific capability was demonstrated by Anan et al. (2019). The DL-NIRSP BiFOIS are the first such devices used in a facility instrument. Images of BiFOIS-36 are shown in Figure 7 to demonstrate the scale and construction of these novel integral-field units. The imaging array, shown in Figure 7d, sits at the final focal plane of the feed optics, while the slit array, shown in Figure 7b, sits at the input focal plane of the spectrograph. Each fiber-optic image slicer is composed of fiber-optic ribbons, making the assembly of a device with so many individual imaging elements feasible. The fiber ribbons are each composed of many cores with a rectangular shape and a buffer of cladding around each fiber core. A microscope view of an illuminated sample of the BiFOIS-36 fiber ribbons is shown in Figure 7c. The individual rectangular cores can be seen in this image.

The DL-NIRSP IFU is located between the polarization modulator and the polarization analyzer (Wollaston prism) in the DL-NIRSP polarimetric system, and in this position it must maintain linear polarization with respect to the polarization directions of the analyzer in the vertical and horizontal directions (i.e. Stokes- Q). Fiber optics do not typically maintain the polarization of light transmitted through them. Slight deformation in an axially symmetric fiber, from manufacturing defects, bending, mechanical vibration, or temperature variation, can easily influence the polarization state of the output light. It is possible to enforce the maintenance of certain polarization states through specification of particular core geometries or stress-induced birefringence in the optical material (see Okamoto, 2006, Section 3 for more detail on this topic).

Schad et al. (2014) demonstrated the linear-polarization maintenance properties of fibers with rectangular cores for the precursor to the DL-NIRSP BiFOIS (and a potential instrument on the JAXA *Solar-C* mission) at 630 nm. This device had a core size of $38 \times 8 \mu\text{m}$ with 1- μm cladding around each core for a total of 2- μm cladding between each fiber core. The extreme aspect ratio between the two core dimensions and the scale of the dimensions with respect to the operating wavelength cause the rectangular fiber to behave as a multi-mode fiber optic in the long dimension and as a single-mode fiber in the short dimension. This behavior contributes to the preservation of linear polarization parallel to the rectangular dimensions of the fiber core.

The size and shape of the fiber core for the DL-NIRSP BiFOIS were selected as a compromise between optimization of plate scale, optical efficiency, intensity cross-talk between fiber cores, and polarization maintenance over the visible to infrared wavelength range of DL-NIRSP. The melting temperatures for the core and cladding glass were also crucial properties to achieve successful fiber fabrication and limited the possible glasses that could be used in this application. The commercially available LF5 glass was used for the core of the fiber, while KG-12 was used for the cladding. The refractive indices of these two glasses become more similar at infrared wavelengths, leading to increased intensity cross-talk at these wavelengths. In addition, these glasses are somewhat absorptive to infrared wavelengths, so keeping the overall length of the fiber ribbons short was important to maintain high throughput.

The BiFOIS for DL-NIRSP are based on a fiber ribbon with a $29 \times 5 \mu\text{m}$ core. The cladding for this device was increased to 3.5 μm for a total of 7 μm of cladding between each

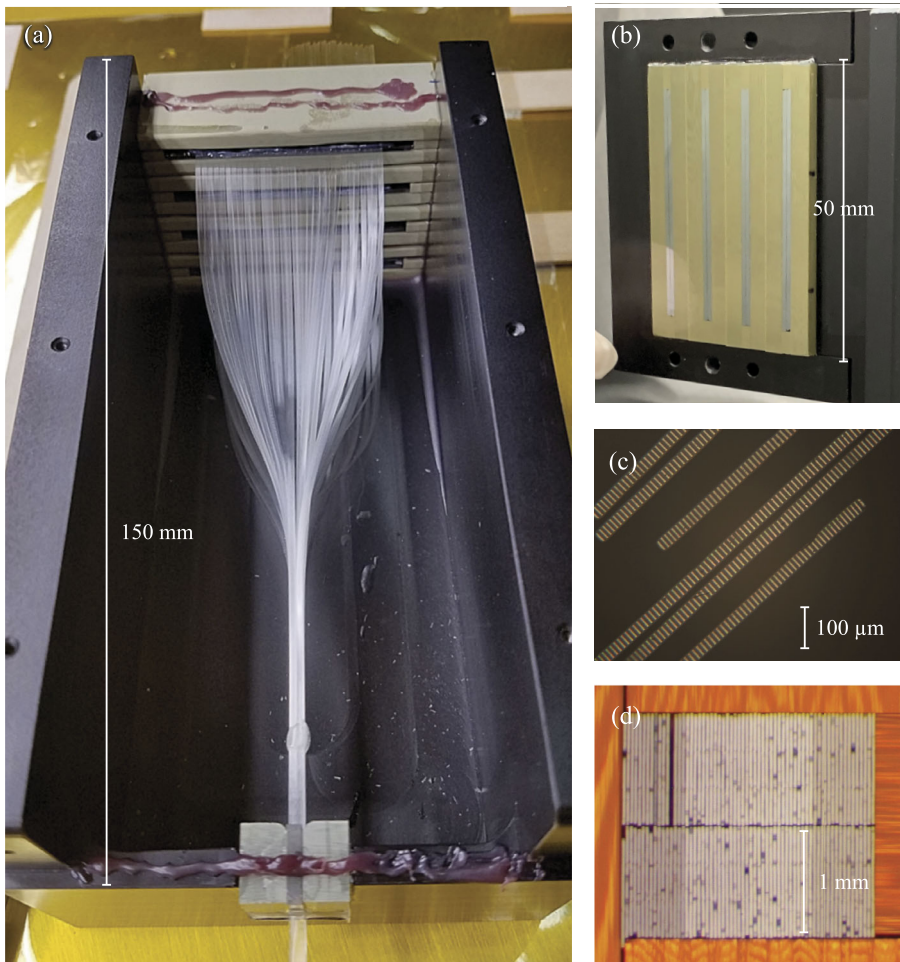


Figure 7 Images of the BiFOIS-36 integral-field unit used for the high- and mid-resolution modes. Panel **a** shows the interior of the mechanical housing during assembly with free-floating fiber ribbons connecting from the densely packed image array (Panel **d**) to the array of four linear slits (Panel **b**). Panel **c** shows a microscope image with the individual fiber cores in each ribbon resolved. Images **a**, **c**, **d** are provided courtesy of Collimated Holes, Inc.

fiber core in the ribbon, in order to decrease the influence of intensity cross-talk between fibers to the level of 3 fibers along the ribbon at 1565 nm. The fiber ribbon for BiFOIS-36 consists of a single column of 90 cores. The core spacing of 12 μm means that three fiber cores are necessary to make one square resolution element, or “imaging pixel.” In the case of BiFOIS-72, the fiber ribbon has been doubled up in both dimensions, with two columns of 180 cores each, and an imaging pixel consists of 6×2 cores. The properties of BiFOIS-36 and -72 are given in Table 5. These numbers are based on the nominal values for the fiber dimensions, but the shape and size of the fiber ribbons are not completely uniform and show some variation.

Table 5 Properties of the IFUs.

IFU	BiFOIS-36	BiFOIS-72
Core Dimensions	29 × 5 μm	29 × 5 μm
Cladding Thickness	3.5 μm	3.5 μm
Ribbon Format	1 × 90 cores	2 × 180 cores
Input Format	64 × 2 ribbons	32 × 2 ribbons
Exit-Slit Height	36 mm	36 mm
Average Exit-Slit Spacing	10.9 mm	10.9 mm
Number of Imaging Elements	64 × 60	32 × 60
Size of Imaging Elements on Sky		
High-Res	0.030''	
Mid-Res	0.077''	
Wide Field		0.464''
Size of Integral Field on Sky:		
High-Res	1.92'' × 1.80''	
Mid-Res	4.93'' × 4.62''	
Wide Field		14.8'' × 27.8''

3.4. Detectors

3.4.1. Arm 1 Balor Camera

DL-NIRSP Arm 1 is equipped with one of the Andor Balor sCMOS cameras specifically developed for DKIST. This device has a detector format of 4128×4104 pixels with square pixels $12 \mu\text{m}$ in size. This same kind of camera is used in VBI and is described further by Wöger et al. (2021). The DL-NIRSP Balor camera is run at a frame rate of approximately 30 Hz to match the frame rate of the infrared cameras. As the spectrograph image magnification is matched to the physical area of the IR detectors, the spectrum fills about 60% of the Balor detector area, so only a portion of the full detector area is read out during standard DL-NIRSP observations. The Balor camera may be run with either a global reset mode or with a rolling shutter. This operational behavior has consequences for modulation of polarization, as described in Section 3.5, and it may impact other aspects of the instrument operation.

3.4.2. Arm 2 and 3 Hawaii-2RGs

The infrared spectral arms of DL-NIRSP, Arms 2 and 3, each use a camera system based on a Hawaii-2RG (H2RG) detector from Teledyne Imaging Systems. The H2RGs are HgCdTe array detectors with 2048×2048 pixels at $18 \mu\text{m}$ pitch. The detectors for DL-NIRSP were intended to have a cutoff wavelength of $2.5 \mu\text{m}$, although they appear to have extended sensitivity; see Section 7. The detectors are cooled to cryogenic temperatures by a closed-cycle Joule–Thomson chiller to avoid local vibration at the camera. There is a fixed cold filter within each cryostat to reject out-of-band light with bandpasses of 880–1370 nm and 1330–1820 nm for Arms 2 and 3, respectively. The H2RGs are read out by University of Hawai‘i supplied STARGRASP controllers (Onaka et al., 2008) at a 29.39-Hz frame rate with a 16-bit ADC sampling resolution.

The readout of the H2RG detector pixels is not simultaneous across the device. They effectively operate in a rolling-shutter mode where each row of pixels is reset and/or read in order. The H2RGs for DL-NIRSP currently have two operating modes implemented depending on the photon flux: “Fast up-the-ramp” and “sub-frame” modes. The fast up-the-ramp mode is used for lower flux situations where the detector does not saturate during one frame time (34 ms), as in the High-Res mode on the disk of the Sun or Wide-Field mode in the corona. During a fast up-the-ramp integration cycle, the detector rows must first be reset and then are immediately read out, producing a bias frame with effectively zero integration time; this process takes one frame time. The detector then integrates charge for one or more integer frame times. The charge in each row is sampled using a non-destructive read (NDR) at the end of the frame time for that row. By making successive NDRs, the effective integration time for that exposure increases. Correlated double sampling and other noise-reducing techniques are possible in this mode. During sub-frame integration, the detector rows are reset and then read out a certain number of row times later, but within a single frame time. Although this style of readout is short, it still incurs a duty cycle of two frame times to reset, integrate, and then read each row. This mode has a minimum exposure length of 0.1 ms (3 sub-frame rows), a maximum exposure length of 34 ms (1023 sub-frame rows), and it is adjustable in units of 0.06 ms (2 rows).

3.5. Polarization System

DL-NIRSP is a dual-beam spectropolarimeter with a rotating waveplate modulator, as imagined by Lites (1987). The major components of this polarization system are the modulator and the polarizing beam-splitter. The modulator encodes the polarized signals as linear polarization during multiple measurements taken during the course of a 180° rotation. The polarizing beam-splitter acts as the analyzer of the encoded linear-polarization signals, converting the linear polarization to intensity signals detectable by the instrument cameras. The beam-splitter simultaneously analyzes orthogonal polarization states in the local Stokes- Q frame of the instrument, in the vertical and horizontal directions. This helps to mitigate any changes in the intensity, due to spatial shifts from atmospheric seeing, instrumental effects, or evolution of solar structure, that occur during the modulation sequence by disentangling them from real polarized signals through combining the two beams during data processing (e.g. Elmore et al., 1992; Casini, de Wijn, and Judge, 2012).

The rectangular fiber cores of the BiFOIS IFUs preserve \pm Stokes- Q linear polarization fairly well, but depolarization and birefringence impact the transmission of other polarization states (see Schad et al., 2014). Thus, the polarization modulator in DL-NIRSP is located just upstream of the IFU in the converging beam from the feed optics. The modulator mixes the desired modulation state into the Stokes- Q state that is preserved by the fibers. The analyzer downstream of the fibers is a “ Q -analyzer,” and all reflections in the spectrograph are in-plane to minimize the influence of polarization cross-talk from Stokes- U and $-V$ into $-Q$ downstream of BiFOIS.

The polarization modulator may be the rotating “waveplate”, as in the modulation scheme imagined by Lites (1987), but it is described more accurately as an elliptical retarder with spatial- and wavelength-dependent parameters. The current DL-NIRSP modulator is actually a spare of the NSO *Coudé Spectropolarimeter* (NCSP: Harrington et al., 2022), and it provides fairly polarimetric efficiency over visible and near-IR wavelengths. The modulator is composed of a five-layer polycarbonate stack sandwiched between the BK-7 entrance and exit windows with index-matching adhesive. (See Harrington et al. (2020) for a full description of the development of this optic.) The modulator-rotation mount and stage was

developed by the NSO for all the polarimetric instruments of DKIST to achieve precise, repeatable rotation with accurate timing (Ferayorni et al., 2014).

The dual-beam polarization analysis must occur close to the camera on each spectral arm to limit the non-common optical path and avoid differential distortion and alignment errors between the two beams. The polarizing beam-splitter, a Wollaston prism, is located in the collimated beam between the collimator and camera lenses of each spectral arm of DL-NIRSP. A Wollaston prism is a bonded pair of right-angle prisms made from birefringent optical crystal where the crystal axis of each prism is orthogonal to the beam-propagation direction and the other crystal axis. A single, unpolarized ray entering the Wollaston is split into two rays with orthogonal linear polarization states (e.g. $\pm Q$). The divergence angle of the two beams is specified by the matching wedge angle of the two prisms and the material index of refraction. In this case, the wedge angle is 34° and the optical material is quartz. The divergence angle is matched to half the separation of the spectra coming from each slit of the IFU, so that the two beams can be dispersed horizontally into the blank space made by the spectral mask.

Spectropolarimetry from DL-NIRSP requires a spatially dependent demodulation of the measured intensity to retrieve the Stokes vector. As with the device described by Schad et al. (2014), the BiFOISs for DL-NIRSP have fiber-to-fiber variation in the polarimetric response. In addition, the operational modes for the detectors (discussed in Section 3.4) have some consequences for the modulation of polarization. The DL-NIRSP modulator is capable of both continuous- and discrete-modulation modes. As the detector pixels for both the visible and IR cameras are read out over the course of one frame time, each row of pixels samples a slightly different modulation cycle during continuous-modulation modes. Therefore, the demodulation matrix for the instrument must be determined on a pixel-by-pixel basis.

3.6. Software

3.6.1. Control System

The operational software for DL-NIRSP is integrated within the software framework of the DKIST observatory (Hubbard, Goodrich, and Wampler, 2010) and reuses many of the same components as other instrument systems. The *Camera Systems Software* provides a standard interface for controlling the DL-NIRSP cameras, including the H2RGs. The high-precision timing of the cameras, modulator, and field-scanning mirror is accomplished using the *DKIST Time Reference and Distribution System* (TRADS: Ferayorni et al., 2014). The *DL-NIRSP Instrument Controller* (IC) is responsible for commanding and sequencing actions of the various mechanisms and cameras within DL-NIRSP. The user interface for this system is the *Instrument Engineering GUI* (IEG). The IEG provides both low-level and high-level control of the instrument. Instrument programs can be run that coordinate the actions of the instrument mechanisms and camera to configure the instrument and run a set of measurements. The instrument operator also has control over individual mechanisms and is provided with their health and status. DL-NIRSP can also be operated in coordination with the telescope and other instruments through the *Observatory Control System* (Johansson and Goodrich, 2012).

3.6.2. Detailed Display and Processing Plugins

The DL-NIRSP operational software includes plugins for processing the data from most observation and calibration tasks. Standard observations are quickly demodulated for polarization and remapped to spatial coordinates to provide quality-assurance data while the

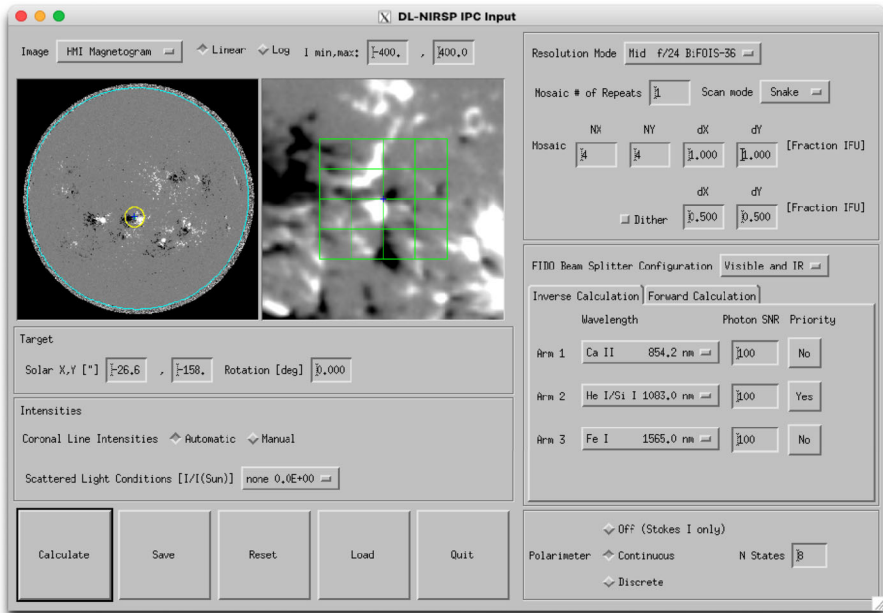


Figure 8 A screenshot from the DL-NIRSP *Instrument Performance Calculator*.

observation is being carried out. Additional processing is carried out for the focus and align tasks, which orchestrate scans of the camera-focus stages and FSM. The images produced by these tasks are analyzed to determine and implement the best focus for the cameras and align the feed optics with respect to a common spatial reference used by all of the instruments.

3.6.3. Instrument Performance Calculator

The DL-NIRSP *Instrument Performance Calculator* (IPC) is a GUI-based tool for determining the operational parameters for DL-NIRSP based on the scientific needs of the end-user. Photon statistics are based on the quiet-Sun radiance and a simple limb-darkening function. Some estimates are currently implemented for coronal use cases, but the user may also input coronal-line intensities in disk-brightness units. This calculation makes use of the estimated instrument efficiency as a function of wavelength discussed in Section 5.3. Example images of the solar disk are provided for determining the approximate size and extent of mosaics. The user can load their own images in FITS format provided they contain standard World Coordinate System (WCS) keywords needed to determine the image scale. Figure 8 shows an example screen shot from the IPC. This tool will continue to evolve as more accurate information on the timing and instrument throughput becomes available, and with changes in the operational model of the instrument. The IPC is currently implemented in IDL[®] and can be obtained from the NSO website for DL-NIRSP, at nso.edu/telescopes/dkist/instruments/dl-nirsp/.

3.6.4. Spectrograph Calculator

The DL-NIRSP *Spectrograph Calculator* is a GUI-based software tool that has been developed to help determine valid spectrograph configurations. The mechanical constraints

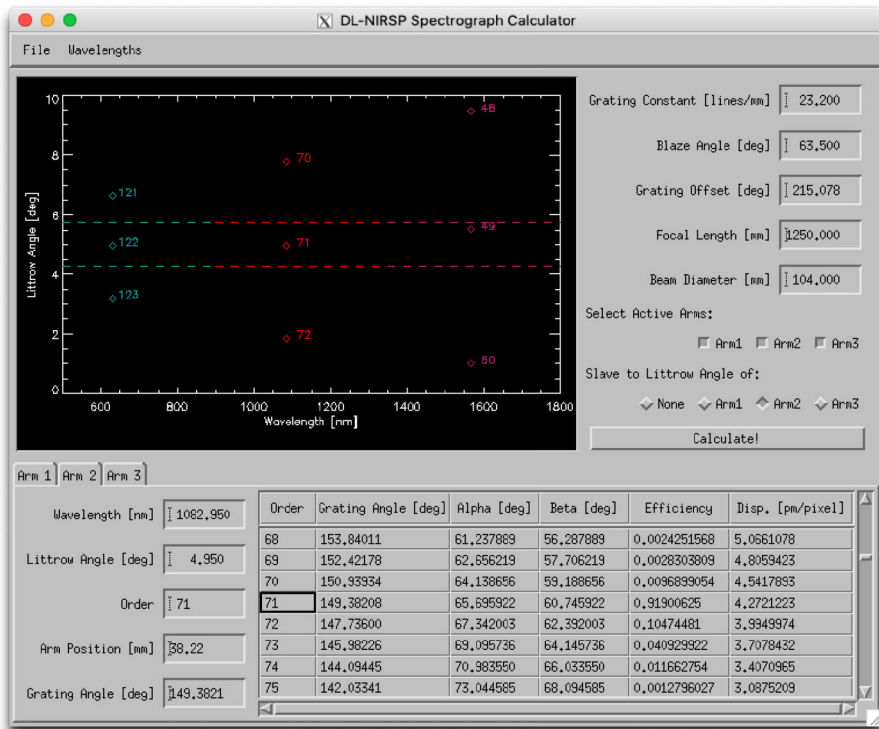


Figure 9 A screenshot of the DL-NIRSP *Spectrograph Calculator* showing the configuration for 630 nm on Arm 1, 1083 nm on Arm 2, and 1565 nm on Arm 3. The blaze orders for each wavelength fall into the valid range of Littrow angles contained within the dashed lines. A blaze angle of 63.5° (rather than the nominal blaze angle of 63°) has been adopted in the spectrograph calculator because the predicted configurations are more consistent with the real performance on the instrument.

provided by the travel range of the spectral arms, the optical constraints from the beam-splitters and the spectrograph OAM vignetting, and the relative positions of the discrete spectrograph orders for the desired wavelengths are combined in a single tool to predict the spectrograph geometry, dispersion, and efficiency. This tool does not take into account the additional limitation of the image quality achieved on each arm of the spectrograph. At the moment, this must be investigated through optical modeling or testing with the actual hardware. A screenshot from the GUI is shown in Figure 9. The *Spectrograph Calculator* is currently implemented in IDL® and can be provided on request for users who wish to explore new wavelength combinations.

4. Optical Alignment

Optical alignment of DL-NIRSP in the DKIST coude lab was achieved using a combination of instruments to achieve high positional and angular accuracy when placing the optics according to an opto-mechanical model. The following description is provided primarily to give the reader insight into the high-precision alignment process and techniques involved in modern optical alignment critical to achieving the spatial and spectral resolution requirements of DL-NIRSP.

The instruments used in the alignment included a laser tracker (FARO[®] Vantage or API Omnitrac2[™]) and a coordinate-measuring machine (CMM) arm (FARO[®] FaroArm[®] or FARO[®] Edge) for measuring distances, a pair of auto-collimating theodolites (Wild-Leica T3000A) for measuring angles between flat optical surfaces, and an optical interferometer (4D Technology PhaseCam[®]6000) with a HeNe (helium–neon) 633-nm wavelength laser for measuring the resulting wavefront shape in the optical system. This combination of instruments allows for mechanical placement at the 20- μ m level and angular accuracy of approximately 30'' in the reflected beam for flat surfaces. The SpatialAnalyzer[®] software by New River Kinematics was used to interface the opto-mechanical model and the measurements from the various devices. Measurements were linked into the global coordinate system of the telescope using the laser tracker to measure the six spherical reflectors located on the structural pillars surrounding the coudé lab with the rotator oriented at zero degrees, and angles were referenced to the DKIST M9 flat mirror through theodolite measurements.

Prior to the optical alignment of the feed optics and spectrograph, the instrument optical tables were located, aligned, and leveled in the context of the coudé opto-mechanical model using a laser tracker. Each component was placed to approximately 0.1 mm accuracy in the horizontal plane of the coudé lab and ≤ 2 mm in height.

4.1. Feed-Optics Alignment

The DL-NIRSP feed optics were aligned first. Each optic was placed using the laser tracker by making measurements on the mount and rear surfaces of the mirrors. The angles of the flat mirrors (Feed FM-2, FM-3, and FM-4) were adjusted with respect to DKIST M9 using the pair of theodolites. Following the initial alignment of the feed optics, the system was tested using the interferometer.

In order to isolate and adjust the powered (non-flat) mirrors, auto-collimated sections of the optical train were created by placing a large flat mirror in a collimated beam and locating a removable spherical reflector at a focal plane with the interferometer just behind it to measure the wavefront error. For example, to align the Feed OAM, the flat mirror was placed at the position of FM-1, and the spherical reflector was placed at the intermediate focal plane with the interferometer between the focal plane and Feed FM-3 looking upstream toward Feed FM-2. Iterative adjustments were made in the interferometer position based on measurements of the spherical reflector and the optical path to ensure that it was in the right position. Then, the tilt and position of the powered optics along the optical path were adjusted to minimize the astigmatism and defocus terms measured by the interferometer.

Finally, the wavefront error of the full optical system from FM-1 to the final focus at the spectrograph was measured for both $f/24$ and $f/62$ modes. The resulting wavefront error, equivalent to a single pass through the system, is shown in Figure 10. The polarization modulator and $f/8$ coronal lens were not included in these measurements.

4.2. Spectrograph Alignment

The Spectrograph FM-1 flat mirror was used as a reference for the placement of all of the spectrograph optics. FM-1 was placed with respect to the spectrograph ISP, then the entire ISP was used to tilt and translate FM-1 in the horizontal plane of the coudé lab with respect to M9 based on laser-tracker and theodolite measurements. The reflective optics of the spectrograph “front end,” including FM-1, the Spectrograph OAM, the diffraction grating, and beam-splitters, were then aligned. The OAM and beam-splitters were placed mechanically.

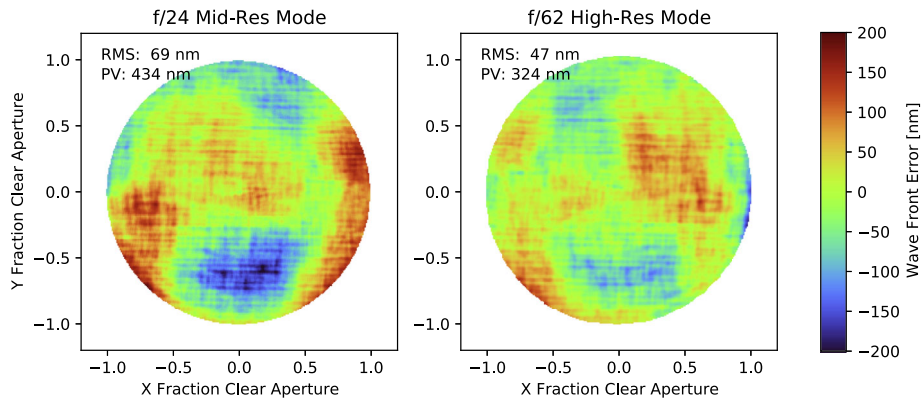


Figure 10 Residual wavefront error of the DL-NIRSP feed optics from the auto-collimating mirror at the FM-1 position to the focal plane at the front end of the spectrograph for the $f/24$ (left panel) and $f/62$ (right panel) branches of the optics following their alignment. The root-mean-square (RMS) and peak-to-valley (PV) values for the residual wavefront error are listed for each case.

A large flat mirror, in place of the diffraction grating, was also positioned using the CMM arm so that interferometric measurements could be carried out. The angles of the grating surrogate mirror and beam-splitters were adjusted using theodolite measurements with FM-1 as a reference. Return spheres were located at the spectrograph input focal plane and intermediate focal plane for Arm 1, and the interferometer was located upstream of the sphere at the spectrograph entrance; then this sphere was removed. The position and tilt of the OAM was then adjusted to minimize the wavefront error for the spectrograph front end.

The wavelength-specific optics made the alignment of the back end of the spectrograph somewhat difficult. While the beam-splitters could be aligned with the CMM arm and theodolite using the reflective front surfaces, it was not possible to use the 633-nm interferometer in the alignment of any of the infrared optics after the beam-splitters due to low transmission and bright surface reflections from the infrared anti-reflection coatings at visible wavelengths. The lens relays for each spectrograph arm were aligned separately using the CMM arm and then placed mechanically as a unit with respect to the rest of the spectrograph. The combined wavefront error of the spectrograph front end and Arm 1 was measured by moving the return sphere at the intermediate focal plane to the final focal plane on Arm 1. The Arm 1 optics were seen to have very little impact on the wavefront error of the system. Figure 11 shows the final measured wavefront error.

Following interferometry, the grating was placed using the CMM arm, and the remaining optics and components were placed by hand or using optical feedback from the detectors, including the detectors themselves, the Wollaston prisms, and the narrow-band filter wheels. To measure the intrinsic optical performance of the spectrograph at representative visible and infrared wavelengths, an array of single-mode optical fibers was used to inject HeNe laser light at various positions across the input focal plane. This synthetic “star-field” was positioned with respect to the spectrograph optics using the CMM arm. The single-mode fibers have a mode-field radius at the level of a few microns depending on the wavelength. In combination with illumination from the HeNe laser, the star-field fibers are point like in both the spatial and spectral dimensions. Any resulting blurring or aberration in the star-field fibers re-imaged by the spectrograph can be attributed to spectrograph wavefront error and diffraction. To characterize each spectral arm of DL-NIRSP, it was necessary to use different HeNe laser wavelengths and single-mode fiber optics specific to these wavelengths.

Figure 11 Residual wavefront error of the DL-NIRSP spectrograph optics from the IFU exit slits to the final focal plane on Arm 1. During this measurement the grating was replaced with a flat mirror, and the Arm 1 position and grating surrogate mirror angle were configured to achieve the smallest wavefront error. The root-mean-square and peak-to-valley values for the residual are listed for each case.

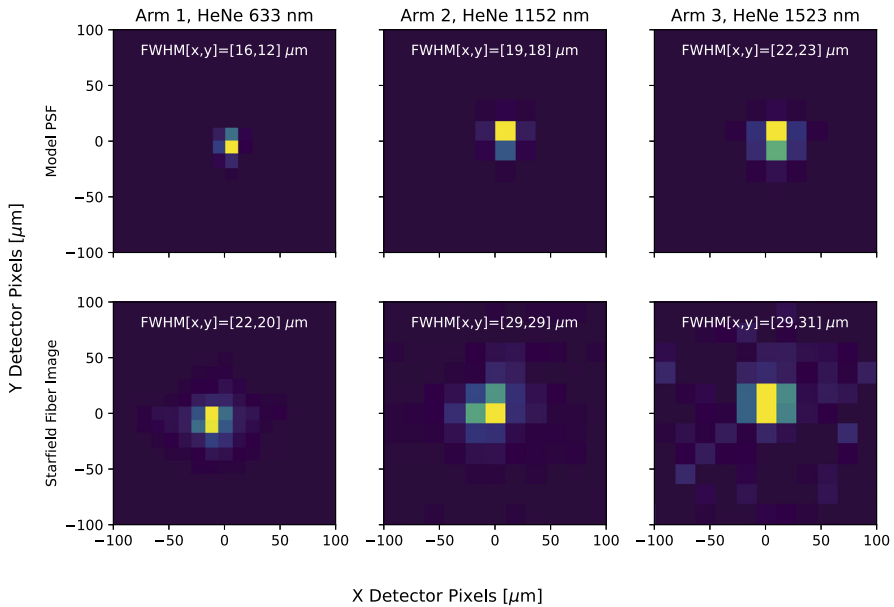
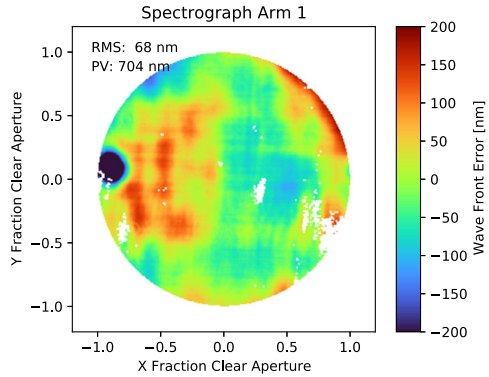


Figure 12 A comparison of the re-imaged “star” from the fiber-optic “star-field” center field position (*bottom row*) with the model PSF of the spectrograph for the corresponding wavelength and configuration (*top row*). The model PSF has been resampled to the same scale as the detector pixels. A 2D Gaussian profile was fit to the resampled model PSF and the observed star-field images, the FWHM in the *x*- and *y*-directions of the fitted profiles are listed at the top of each panel.

HeNe lasers with wavelengths of 633 nm, 1152 nm, and 1523 nm were used to characterize Arms 1, 2, and 3, respectively. Image quality in the spectrograph is highly sensitive to the configuration, as defined by the grating angle and spectral arm position, so for each HeNe laser wavelength, the spectrograph was stepped through various configurations to locate the one with the best performance. Figure 12 shows the best imaging performance achieved for each arm in comparison with the theoretical prediction of the point spread function (PSF) of the spectrograph for these wavelengths. The measured star-field spots have a width that is about 1.5 times larger than the model PSF.

Following the star-field measurements, IFU-36 was placed with the CMM arm. The spectral masks were placed to achieve optimal wavelength centering and focus as seen by the camera for each arm. The modulator was placed using the CMM arm, and tip/tilt of the assembly and modulator cell was carried out using a reference theodolite. The tip and tilt of the modulator optical cell inside the rotation mount must compensate for beam deflection by using a specific tilt angle as well as minimizing beam jitter. Some residual beam displacement at the IFU focal plane is still apparent after the initial alignment. We anticipate improvement with further alignment efforts.

5. As-Built Performance

The performance of DL-NIRSP has been tested using a combination of observations with sunlight, the calibration lamp and targets at the *Gregorian Optical Station* (GOS: Rimmelé et al., 2020), and various calibration sources set up within the coudé lab during the instrument-commissioning phase. The following sub-sections provide results and discussion on the major aspects of the instrument performance, including the spatial and spectral resolution, wavelength coverage and throughput, polarization performance, instrument stability, and the combinations of wavelengths achievable by the spectrograph.

5.1. Spatial Resolution

An accurate end-to-end characterization of the spatial resolution of DL-NIRSP has been, so far, difficult to obtain. There are many factors that contribute to the spatial resolution that DL-NIRSP can achieve, including the wavefront error of the spectrograph and feed optics, fiber-to-fiber cross-talk within the BiFOIS IFU, and the stability within the DL-NIRSP and DKIST optical paths. The measurements of the DL-NIRSP feed optics and spectrograph wavefront error made during the optical alignment (Figures 10 and 11) are within their budgeted tolerance and confirm that these optical trains are performing at the level required to deliver diffraction-limited performance. Additional measurements of the image quality internal to the spectrograph were necessary to characterize the optical performance in the infrared, because the interferometric measurement only works for the visible-wavelength optics. The star-field images in Figure 12 demonstrate that the intrinsic behavior of the spectrograph is within budget and close to ideal for the most part. This testing showed that the Wollaston prism on Arm 2 contributes to poor imaging performance on this arm. Fabrication of a new Wollaston prism for this arm is currently underway.

We propose two strategies for determination of the DL-NIRSP spatial resolution that may be carried out in the near future. The first task is to determine the combined spatial resolution of the spectrograph and the IFU. This can be done using the same calibration data set necessary to spatially remap the spectrograph images. During this calibration, images are taken while a knife edge located at an image plane is scanned across the IFU entrance in the horizontal and vertical directions. Lin and Versteegh (2006) and Versteegh (2006) demonstrated how this technique might be used to spatially reconstruct spectra from an IFU, a by-product of the calibration is a characterization of the profile of the knife edge, which is directly related to the imaging performance. The current IFU remapping calibration was performed with the knife edge located at the intermediate focus in the feed optics, but as noted before, this focus has astigmatism, and the characterization of the spatial mapping and imaging performance is not adequate. We propose to modify this calibration by placing the knife edge directly in front of the IFU entrance surface, as was done by Versteegh (2006).

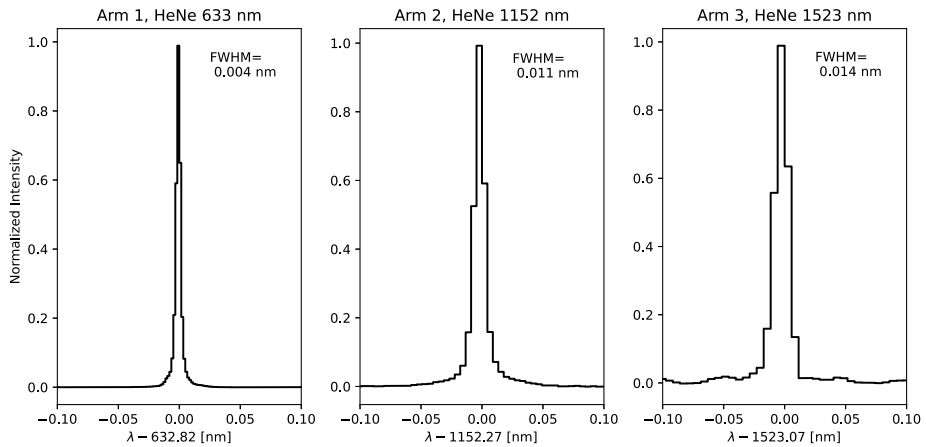


Figure 13 The average spectral profile of the spectrograph with BiFOIS-36 measured using spectral arms 1, 2, and 3 with input HeNe laser light at 633, 1152, and 1523 nm, respectively. The equivalent FWHM of a Gaussian fitted to the profile is shown in the upper right of each panel.

The slow focal ratio of DL-NIRSP allows for slight offsets in the focus direction, so the knife edge may be placed immediately in front of the IFU to perform this scan.

For the evaluation of the full performance of DL-NIRSP, the Sun provides many spatially compact features, as seen in observations from VBI (Wöger et al., 2021). By observing these features with AO simultaneously with the VBI blue- or red-continuum channel and DL-NIRSP, the end-to-end spatial resolution of DL-NIRSP, including the telescope, DL-NIRSP feed optics, and the spectrograph can be derived. These two techniques combined should allow us to isolate sources of image-quality degradation in the system.

5.2. Spectral Resolution

The spectral resolution of each arm of the DL-NIRSP spectrograph with BiFOIS-36 in place was measured using the HeNe laser set described in Section 4.2. Collimated laser light was input into the front end of BiFOIS-36, and although the input was collimated this still leads to a divergent beam exiting the IFU due to focal-ratio degradation. The spectrograph was configured specifically for each arm, using the configurations determined during the star-field testing that achieved the best image quality. The narrow-band filter was removed to allow the laser wavelength to reach the camera. A scan through focus was performed using the focus stage for the camera, and images were taken at each focus stage position. The approximate dispersion for each arm configuration was estimated using the DL-NIRSP spectrograph calculator. Figure 13 shows the average spectral profile measured for each wavelength. This profile was fit with a Gaussian profile to obtain the full width at half-maximum (FWHM). The FWHM of the fitted Gaussian profiles implies equivalent spectral resolving powers of $R = 158,000$ for 633 nm, $105,000$ for 1152 nm, and $109,000$ for 1523 nm using BiFOIS-36. These are slightly lower than the $R = 184,000$, $132,000$, and $120,000$ theoretical resolution of the three wavelengths determined using the Nyquist sampling theorem for infinitely narrow slits, and they can be expected due to the broadening of the spectrum due to the $\approx 29 \mu\text{m}$ width of the fiber core.

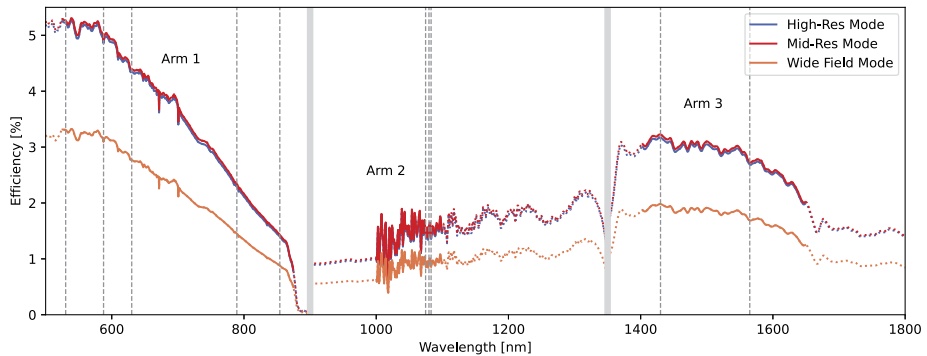


Figure 14 The wavelength coverage of DL-NIRSP with the estimated telescope and instrument efficiency assuming a FIDO configuration that allows 500 nm and longer to pass to DL-NIRSP. Wavelength data are not available for all optics over the full wavelength range, *dotted lines* show where some of the data have been extrapolated. The *gray dashed lines* indicate the wavelengths of the current set of narrow-band filters. The transmission of these filters is not included in the estimated efficiency but is typically better than 80% (see Figure 15). The *gray bands* indicate the boundaries of wavelengths between each arm.

5.3. Wavelength Coverage and Throughput

Measurement of the end-to-end throughput of DL-NIRSP, or any astronomical instrument, as a function of wavelength would require extensive observations of a bright external calibration light source with known spectral brightness, and cannot be done easily. Therefore, the final estimate for the radiometric throughput of the combined DKIST and DL-NIRSP optical path was prepared based on a combination of vendor-provided information, measurements made using UH/IfA and NSO facilities, and estimates based on the material properties (if no other information was available). This estimate includes detailed wavelength-dependent surface reflectivities, coating and bulk transmission factors, as well as the detector quantum efficiencies. The items with the largest associated uncertainty are the absolute transmission efficiency of the BiFOIS and the grating efficiency for the particular spectrograph configuration that DL-NIRSP will use. The estimated radiometric efficiency of each spectral arm is shown in Figure 14. Some of the transmission and reflectivity data were not available at all wavelengths and were extrapolated to the edge of the bandpass for each spectral arm. These regions are indicated by the dotted lines in the figure and should be considered as an upper limit on the efficiency.

The transmission profiles of the narrow-band filters are not included in the above estimate, but they typically have in-band throughput over 80%. Figure 15 shows the detailed transmission profiles measured for each of the narrow-band filters currently available for DL-NIRSP. For context with respect to the solar spectrum, the atlas spectrum from the NSO *Fourier Transform Spectrometer* is shown (Kurucz et al., 1984). Some of the high-frequency ripples that can be seen in a few of the filter profiles may be due to changes in the instrumental setup between the filter and reference measurements.

These filters control the accessible bandpass, while the bandwidth is set by the dimensions of the slots in the spectral mask. It is possible to intentionally offset the center wavelength of the spectrum transmitted by the spectral mask from the filter bandpass to access different regions of the spectrum, the risk is that light from the wings of the filter profile may start to contaminate the spectra from neighboring slits. The center of the filter bandpass may also be adjusted slightly from those shown. The center of the bandpass can be

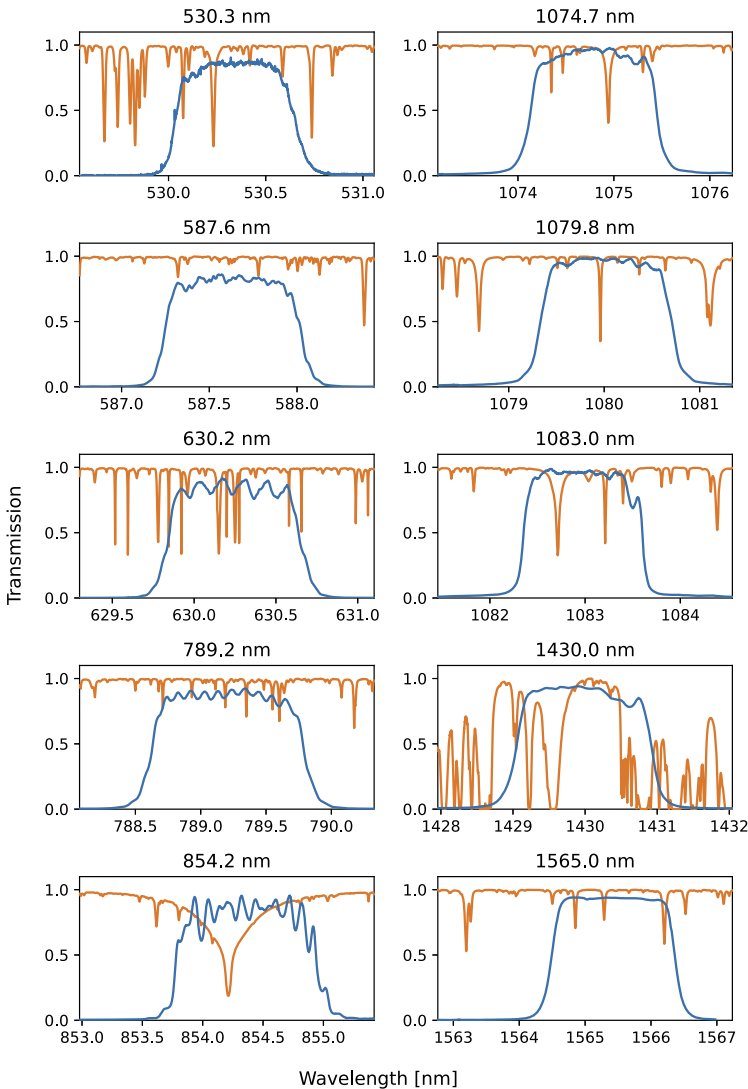


Figure 15 The measured profiles for each of the DL-NIRSP narrow-band filters. The filter transmission is shown in *blue* and the NSO FTS atlas spectrum in normalized intensity units, shown in *orange*, is provided for context in each waveband. Note that the center wavelength of the bandpass can be adjusted toward short wavelengths with small adjustments of the angle of incidence of the beam.

adjusted with slight changes in the angle of incidence, which shift the bandpass to shorter wavelengths.

The combined throughput estimate is used in the instrument performance calculator to determine the photon flux at the DL-NIRSP detectors for different configurations.

5.4. Polarization

One of the limiting factors in achieving high signal-to-noise spectropolarimetry is the polarization performance of the telescope and instrument optical system. If depolarization is

present in the telescope or instrument optics, or if the modulation is not efficient, then more photons are needed to achieve equivalent polarimetric signal to noise. This is especially important for coronal measurements where the polarized signals are a small fraction of the total intensity signal. The DKIST optics and DL-NIRSP feed optics have been rigorously characterized and are well described as non-depolarizing (Harrington and Sueoka, 2018; Harrington, Sueoka, and White, 2019; Harrington et al., 2021), and the DL-NIRSP spectrograph has been designed to maintain the local Stokes- Q linear-polarization state, but the Bi-FOIS IFU can potentially impact the modulation efficiency. The modulation scheme for DL-NIRSP is based on a rotating modulator that mixes the desired state into the local Stokes- Q frame, which is analyzed by the Wollaston prism downstream. The IFU is placed between the modulator and analyzer, and thus any depolarization or transfer of Stokes- Q into circular polarization by the IFU results in degraded performance. The wavelength-dependent performance of the modulator can also impact the efficiency, although it is reasonably well balanced between 40% and 70% for ξ_Q , ξ_U , and ξ_V (see Figure 48 in Harrington et al., 2020).

The modulation efficiency of DL-NIRSP was calculated using a data set obtained for modulation calibration using the GOS fused-silica wire-grid polarizer and the optically contacted retarder. This calibration was carried out on 05 August 2021 during the science-verification observations using the 630-, 1083-, and 1565-nm channels for Arms 1, 2, and 3, respectively. The modulation matrix was determined pixel-by-pixel for each of the DL-NIRSP spectral arms (see Harrington et al., 2022, for more details on how this is derived), and then from this the optimal demodulation matrix and modulation efficiency [ξ] were calculated for each of the Stokes-vector components using Equations 5.28 and 5.29 from del Toro Iniesta (2003). The pixel-by-pixel modulation efficiency is shown in Figure 16. Some regions of the spectra have low signal and produced invalid results; these regions have been set to zero in the figure. For an ideal system, the modulation efficiency $\xi_I = 1$ and $\sqrt{\xi_Q^2 + \xi_U^2 + \xi_V^2} = 1$. For this spectrograph configuration of DL-NIRSP, the average modulation efficiency is greater than 0.75 for Stokes- I and greater than 0.65 for the combined polarized states. Considering only the modulator and using the wavelength-dependent characterization of Harrington et al. (2020), we estimate an efficiency of greater than 0.85 for Stokes- I and greater than 0.90 for the combined polarized states for an 8-state modulation cycle over the same set of wavelengths. The polarization performance may change significantly as a function of wavelength, so the measurements shown here are not necessarily representative of the other wavelengths of DL-NIRSP.

5.5. Stability

Stability of the DL-NIRSP spectrograph and feed optical path are critical to achieving spatial resolution and polarimetric accuracy. Mechanical drift within the spectrograph can cause changes in the instrument flat field, which may introduce intensity errors if these occur within the time between the calibrations and science observation. Mitigating changes in the flat field may demand frequent recalibration, reducing the operational efficiency. The large variation in the fiber-to-fiber transmitted intensity through the BiFOIS IFUs, as well as the edges of individual ribbons, can also exacerbate any small shifts in the spectra with respect to the detector pixels.

Image drifts within the spectrograph and in the feed optics of DL-NIRSP were characterized over a time period of a few minutes using observations of the solar spectrum. To measure image drift within the spectrograph, the telescope was targeted on quiet Sun near

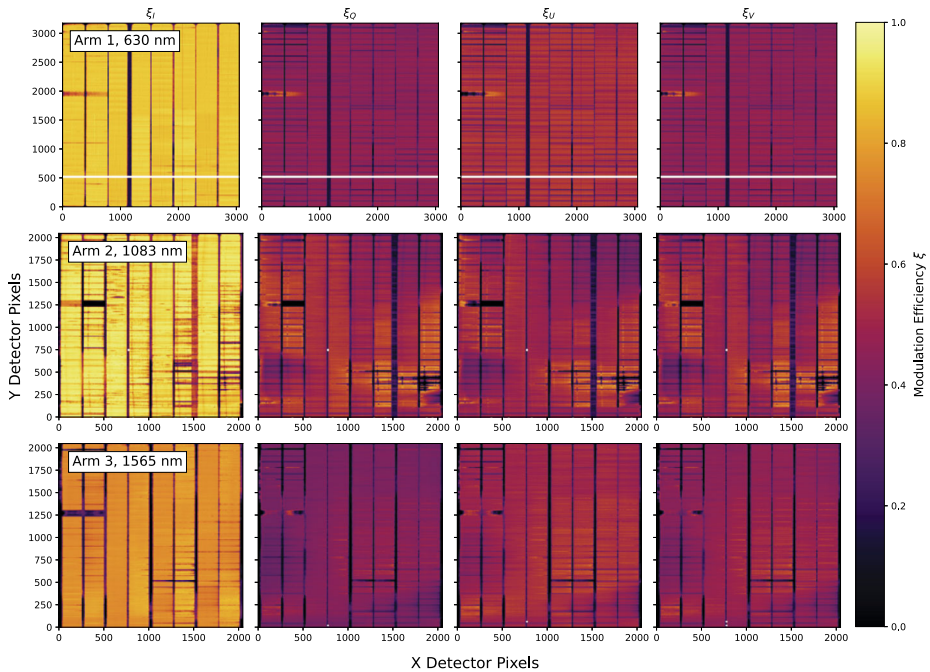


Figure 16 The modulation efficiency of the three DL-NIRSP spectral arms at wavelengths of 630, 1083, and 1565 nm using the eight-state modulation sequence. The efficiency $[\xi]$ for each of the Stokes-vector components (I , Q , U , V) is as defined by del Toro Iniesta (2003) Equation 5.29 for an optimal demodulation matrix.

the center of the solar disk. Images were collected continuously for about eight minutes using the 630/1083/1565-nm spectrograph configuration for DL-NIRSP. In the resulting image series from each spectral arm, a cross-correlation technique was used to derive the shift of each image in the x - and y -directions with respect to a reference image. Figure 17 shows the resulting image shifts measured, converted to microns. The shifts derived from Arms 1 and 3 show consistent behavior, with RMS shifts of 2–3 μm . The shifts from Arm 2 are likely impacted by the image-quality issue described in Section 4.2.

Stability of the image on the DL-NIRSP IFU was also measured. In this case, the telescope was still illuminated with sunlight. A pinhole field stop was put into the beam at GOS, and the HOAO was locked onto the pinhole to provide a correction for any motion between GOS and DKIST M10. A series of observations was run continuously over a few minutes using the DL-NIRSP 630/1083/1565-nm spectrograph configuration for both High- and Mid-Res modes. The polarization modulator was not run, as it introduces an additional beam wobble that will be corrected in the future. In the resulting image series from each spectral arm of DL-NIRSP, the images from the spectrograph were spatially reconstructed using the preliminary mapping from the knife edge scan (see Section 5.1). The center of the pinhole was determined in the reconstructed image, this is shown in Figure 18. Some scatter here may be attributed to poor performance of the reconstruction, although the scatter is slightly larger in the High-Res mode, this is to be expected because the magnification is 2.6 times larger than for the Mid-Res mode. The high-frequency jitter may be mechanical or it may be optical, i.e. due to air currents or “seeing” in the coude lab between the adaptive-optics deformable mirror (DKIST M10) and the focal plane of the DL-NIRSP feed optics.

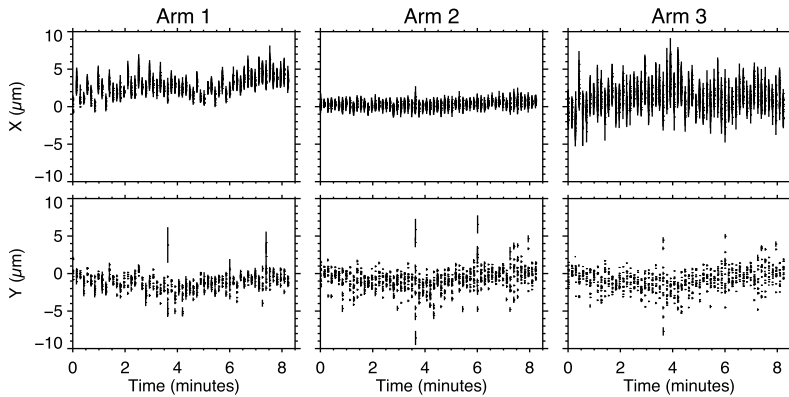


Figure 17 Shifts of solar spectra for Arms 1, 2, and 3 as a function of time.

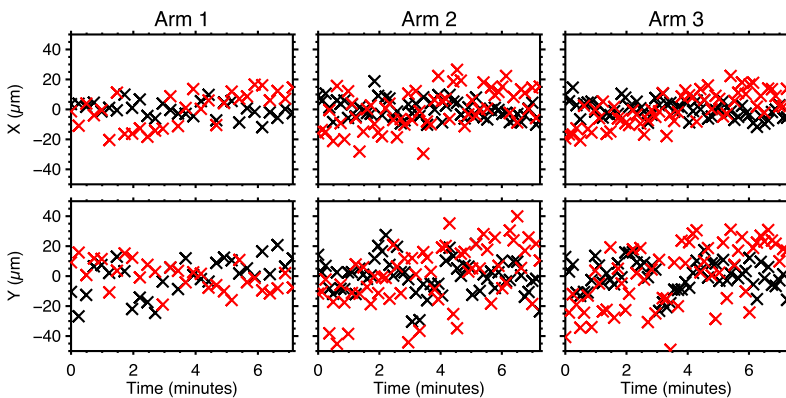


Figure 18 Shifts in the measured pinhole position with respect to the IFU as a function of time. The *red crosses* show the pinhole drift in High-Res mode, while the *black crosses* show the drift in Mid-Res mode over the same length of time, although the data were not collected simultaneously. In both cases, $36\ \mu\text{m}$ is equivalent to one imaging pixel, and the corresponding scale on the sky is defined for each mode in Table 5.

The systematic drift in these relatively short time series is likely mechanical. The long-term stability of DL-NIRSP is known to be impacted by rotation of the coudé laboratory; this has not yet been characterized, but is forthcoming.

5.6. Spectrograph Configurations

The DL-NIRSP spectrograph is configurable for different wavelength combinations, but these configurations are in fact highly constrained. Configurations that stray too far from the nominally designed Littrow angle for each arm can suffer from degradation of spatial and spectral resolution and reduced intensity due to vignetting on the Spectrograph OAM and dichroic beam-splitters. In order to observe different wavelengths together, the desired spectral order for each arm must fall into the correct range of Littrow angles. Combinations with $1079.8\ \text{nm}$ on Arm 2 and $1430.0\ \text{nm}$ on Arm 3, or $1074.7\ \text{nm}$ on Arm 2 and $1565.0\ \text{nm}$ on Arm 3 may not be possible because these require a configuration

Table 6 Three-Wavelength Spectrograph Configurations.

Wavelength [nm]			Notes
Arm 1	Arm 2	Arm 3	
Photosphere and Chromosphere			
630.2	1083.0	1565.0	tested
587.6	1083.0	1565.0	tested
854.2	1083.0	1565.0	tested
Corona			
530.3	1074.7	1430.0	Arm 1 order+1
789.2	1074.7	1430.0	tested
Mixed			
587.6	1074.7	1430.0	
630.2	1074.7	1430.0	Arm 1 blaze order +1
854.3	1074.7	1430.0	Possible with reduced throughput for Arm 1 and 3
530.0	1079.8	1565.0	
587.6	1079.8	1565.0	
630.2	1079.8	1565.0	
789.2	1079.8	1565.0	Arm 1 blaze order -1
854.2	1079.8	1565.0	
530.0	1083.0	1430.0	
587.6	1083.0	1430.0	
630.2	1083.0	1430.0	
789.2	1083.0	1430.0	Possible with reduced throughput on Arm 1
854.2	1083.0	1430.0	
530.3	1083.0	1565.0	
789.2	1083.0	1565.0	Arm 1 blaze order -1

that falls outside of the proscribed limits on the Littrow angle due to the wide spacing of the infrared orders. The efficiency of the blazed grating causes intensity to be more tightly confined to the blaze order. Conversely, toward shorter visible wavelengths, the orders are closer together and orders ± 1 about the blaze order still show significant efficiency.

Table 6 lists possible three-wavelength configurations for the current grating and filter set. These combinations could also be optimized for any two wavelengths, and it is always possible to use one wavelength with the optimal configuration for that arm. These configurations were determined using the DL-NIRSP *Spectrograph Calculator* described in Section 3.6.4. Configurations that have been tested successfully on the instrument hardware are listed as “tested.”

6. First Results

6.1. A Pore in the Photosphere

DL-NIRSP observed the largest pore in the leading polarity of active region NOAA 12851 on 05 August 2021 starting at 21:55:41 UT. The DKIST wavefront-correction system was

used to lock on the pore and correct for atmospheric seeing. The 630/1083/1565-nm spectrograph configuration was used with the Mid-Res mode. A 7×7 mosaic was taken using 4.69'' steps of the field-scanning mirror in both the x - and y -directions, covering a full field of view of approximately $30'' \times 30''$. This mosaic took approximately two minutes to conduct and was repeated four times. During each step in the mosaic, DL-NIRSP obtained full-Stokes polarimetry using the eight-state continuous-modulation scheme. The necessary calibration data, including darks, flats, and polarization calibration, were taken on the same day.

A preliminary reduction was performed for the spectropolarimetric data to subtract dark levels, remove flat-field effects, and retrieve the Stokes vector. From the reduced data set, we derived quantities based on the line and continuum properties and then reconstructed these quantities spatially using the knife edge mapping calibration of the IFU. Figure 19 shows the reconstruction from the first repeat of the mosaic observations taken with DL-NIRSP. For each spectral-arm channel, we show the derived continuum intensity and the Doppler velocity and Stokes- V amplitude based on the main photospheric line in each channel (Arm 1: Fe I 630.25 nm, Arm 2: Si I 1082.71 nm, Arm 3: Fe I 1564.85 nm). Figure 20 shows how this pore appeared in the continuum intensity, Doppler velocity, and magnetic-field strength data products from the *Solar Dynamics Observatory/Helioseismic and Magnetic Imager* (SDO/HMI: Pesnell, Thompson, and Chamberlin, 2012; Schou et al., 2012) taken near the same time as the DL-NIRSP observations.

This set of reconstructed quantities shows consistent physical behavior between the various channels and they are in excellent agreement with the HMI quantities. Although diffraction-limited resolution decreases with wavelength, the 1565-nm infrared channel actually shows the highest spatial resolution for this observation. The atmospheric conditions were moderate to poor, and the resolution of the observation is still largely dominated by seeing. The impact of seeing is greatly reduced at infrared wavelengths. Artifacts from the mosaic reconstruction are apparent, especially in the images from the IR cameras (Arms 2 and 3). Work on the mosaic reconstruction is ongoing.

6.2. Active-Region Corona

DL-NIRSP made observations of the corona on 07 August 2021, using the Mid-Res mode because the Wide-Field mode was not yet available. DKIST was pointed to target the corona at $1.2 R_{\odot}$, above active region NOAA 12853 when it was on the east limb. The white star on the left side in Figure 21 shows the approximate location of the observation in the context of SDO's *Atmospheric Imaging Assembly* (AIA: Lemen et al., 2012) image taken near the same time as the observations. The DKIST Lyot stop was in place between DKIST M2 and M3 during these observations, and because this observation was off the solar disk, no wavefront correction was possible. DL-NIRSP started observations at this location starting at 21:36:34 UT using Mid-Res Mode with the 789/1075/1430-nm wavelength configuration and eight-state discrete-mode modulation. These observations only lasted about two minutes, including the delays for discrete modulator motion. The individual exposures of the IR camera amount to approximately seven seconds of integration. An identical observation was made at $1.2 R_{\odot}$ at the north limb of the Sun, indicated by the white star in the upper right of Figure 21. Measurements were also taken at the Sun center to calibrate the intensity level of the coronal observations.

A preliminary calibration and data reduction was performed for this data set. All of the modulation states and repeats from each location were summed together. The north-pole measurement was subtracted from the active-region measurements assuming that the north pole should show a very small signal from the coronal emission lines and primarily contains

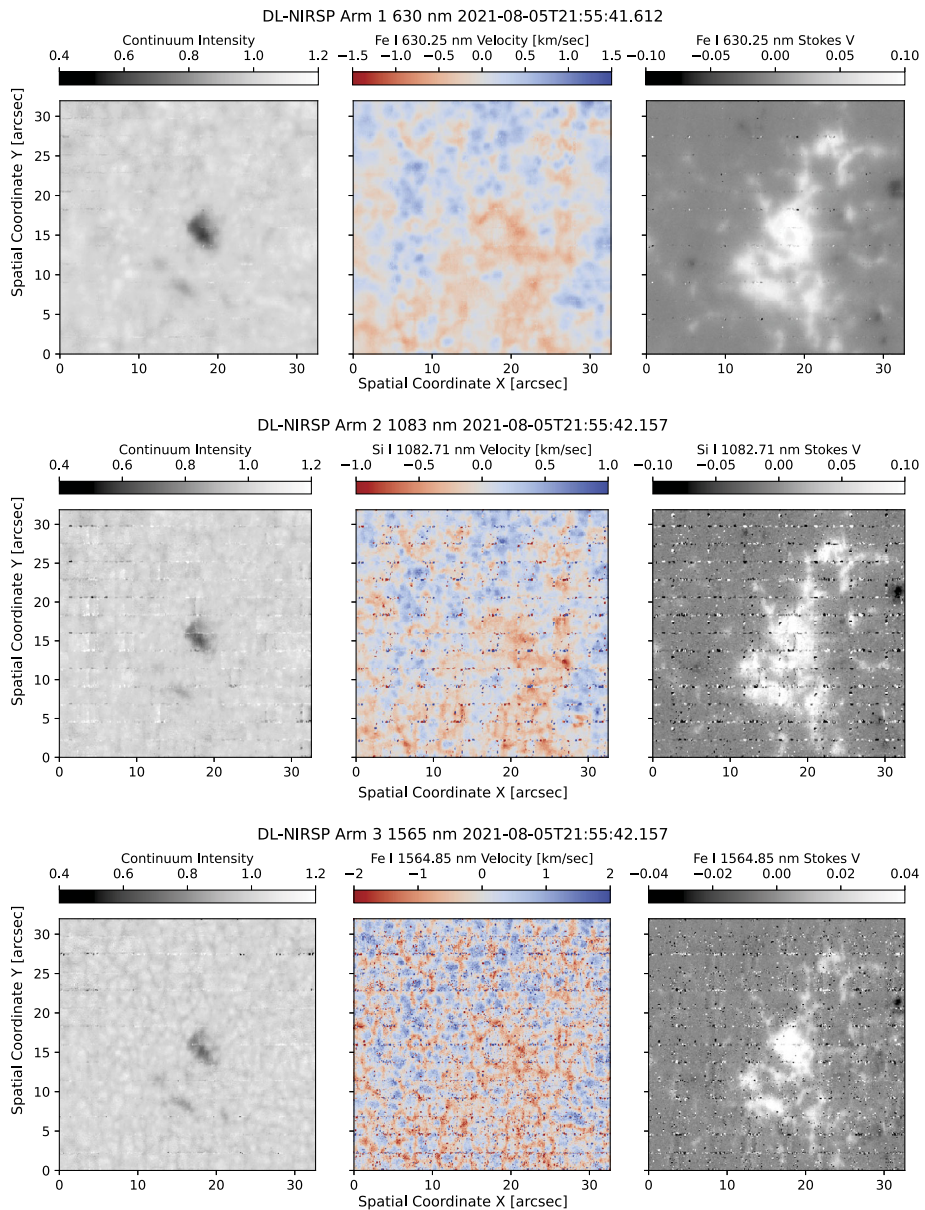


Figure 19 The spatially reconstructed continuum intensity, Doppler velocity, and LOS magnetic field of the leading pore in NOAA 12851 derived from a spectropolarimetric mosaic using the 630-, 1083-, and 1565-nm channels of DL-NIRSP. Artifacts from the mosaic reconstruction are apparent, especially in the images from the IR cameras.

the background signal composed of scattered light from the solar disk due to the Earth's atmosphere and from the telescope, as well as the coronal continuum. The coronal-emission-line spectra for each arm were shifted in wavelength and averaged together to create the

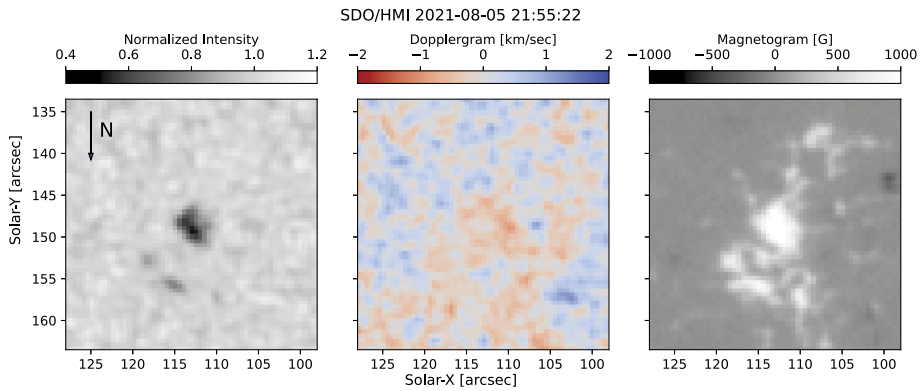
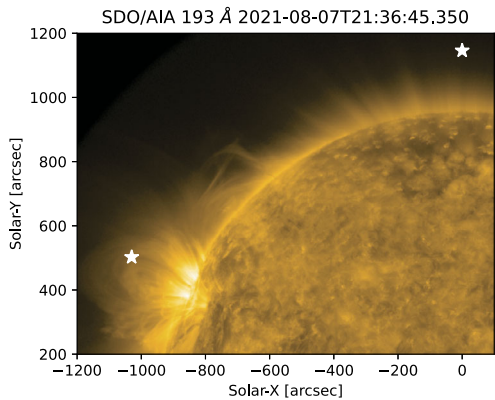


Figure 20 An HMI cutout of the leading pore in NOAA 12851 covering the approximate region observed with DL-NIRSP. The HMI images have been rotated so that solar north is down to match the orientation of the DL-NIRSP maps.

Figure 21 A portion of the AIA 193-Å image taken near the time of the DL-NIRSP coronal observation. The stars indicate the approximate observed locations at $1.2 R_{\odot}$ in the corona over the active region and the Sun’s north pole.



profiles shown in the top row of Figure 22. The same shifting and averaging was applied to the spectra before background subtraction to show the total signal level in the observation; these are shown in the bottom row of the figure.

NOAA 12853 was a fairly weak active region with no noticeable sunspots once it was fully visible on the disk of the Sun. It should also be noted that these observations were taken with DL-NIRSP in a mode that was not specifically intended for coronal measurements. Despite these obstacles, the observations show unambiguous detections of the [Fe XI] line at 789.2 nm, the [Fe XIII] line at 1074.7 nm, and even the [Si X] line at 1430.0 nm, which has previously been very difficult to detect in ground-based observations (Penn and Kuhn, 1994; Dima, Kuhn, and Schad, 2019).

7. Conclusions and Outlook

Each instrument in the first-light suite of DKIST has different strengths. As an integral-field spectropolarimeter, DL-NIRSP is the only DKIST instrument capable of obtaining simultaneous spatial and spectral information over a continuous 2D field of view. Its three simulta-

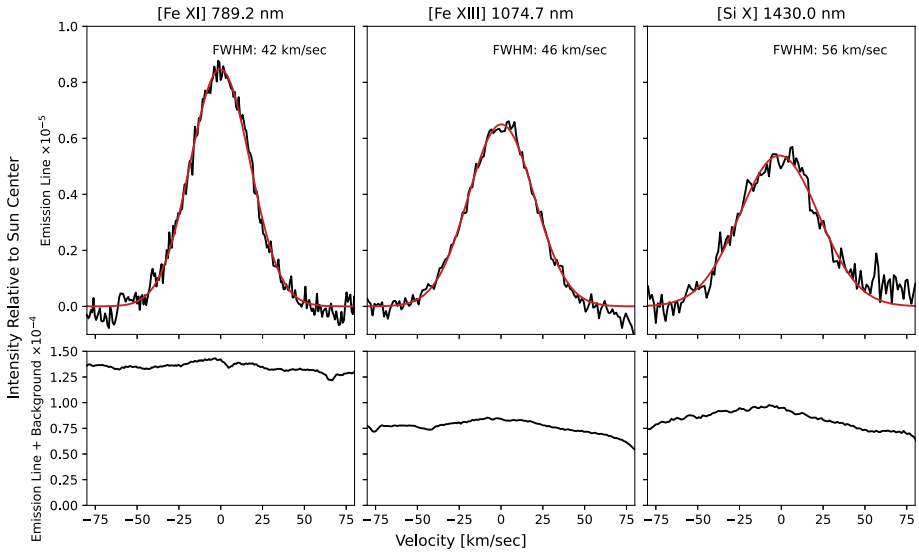


Figure 22 Average coronal spectra $1.2 R_{\odot}$ over active region NOAA 12853 measured with DL-NIRSP in Mid-Res Mode. The wavelength scale has been converted to velocity units. The *upper set of panels* shows the coronal emission-line profiles after background subtraction. The line profiles were fitted with a Gaussian profile (*red line*) and the FWHM is listed in the *upper right*. The *lower set of panels* shows the total measurement with the coronal emission line, coronal continuum, and scattered-light background contributions.

neous spectral channels target specific photospheric, chromospheric, and coronal diagnostics at visible and infrared wavelengths that allow for observation of the polarized signatures of the Sun's magnetic field with high spectral resolution. It has a scanning mirror and three spatial-resolution modes that allow for mosaics of regions up to $2' \times 2'$ with different plate scales. DL-NIRSP's highly flexible design allows the user to make trade-offs between sensitivity, cadence, spatial resolution, and field-of-view coverage to optimize for many different science use cases, from diffraction-limited observations on-disk to sensitive observations in the solar corona. DL-NIRSP receives the AO-corrected beam from the DKIST wavefront-correction system and can operate alongside the other first-light instruments.

Many of the components of DL-NIRSP provided a technical challenge that pushed the boundaries of what is possible for an instrument. DL-NIRSP incorporates custom components, including the novel fiber-optic integral field units, high-performance narrow-band filters, precision mechanisms, as well as camera systems specifically developed for this application. The optical design including off-axis mirrors was met with a high-precision alignment process to achieve the necessary wavefront-error goals. While the performance of the instrument is still being understood, DL-NIRSP has been used to carry out its first solar observations of a magnetic active region on the solar disk and over an active region in the corona. These first disk and coronal observations with DL-NIRSP show promise and set the stage for future studies.

Although DL-NIRSP has only just been completed, there are already many major improvements and upgrades planned that will be implemented during early operations with the instrument. The most exciting and impactful of these upgrades is the implementation of the *Machined Image Slicer* IFU with a $36\text{-}\mu\text{m}$ slit width (MISI-36) to replace BiFOIS-36. Functionally similar to the polished-glass image slicer for GRIS (Dominguez-Tagle et al., 2022), MISI-36 would have spatial sampling and FOV equivalent to BiFOIS-36 but would

have nominally three times higher throughput, with better intensity uniformity and polarization fidelity relative to the fiber-based IFUs. Although the improved throughput would make it possible to use the Mid-Res mode in the corona, an image slicer with coarse spatial sampling is also in development for coronal observations.

Additional optical development will address issues discovered during the construction and commissioning of the instrument. The excess wavefront error due to the Wollaston prism on Arm 2 will be addressed with fabrication of a new component so that this channel will achieve its expected spatial and spectral resolution. The H2RG detectors were found to have residual sensitivity far beyond the 2.5- μm cutoff wavelength of the detectors and well past the 3- μm blocking provided by DL-NIRSP's current cold filters (known as an Urbach tail: Terrien et al., 2016), and they require new cold filters with extended blocking out to 5 μm . Polarized fringes are apparent in the infrared channels of DL-NIRSP when using the High-Res mode. As the current DL-NIRSP modulator is a spare calibrator from a laboratory system, it was not optimized specifically as a modulator, and fringe suppression was not a consideration during the design (see Harrington and Sueoka, 2018; Harrington et al., 2020). A new polycarbonate modulator with coatings and window thicknesses designed to suppress fringe frequencies visible to DL-NIRSP is in fabrication.

DL-NIRSP provides coverage of a fixed set of wavelengths, and the ability to do this depends on the filter set and the ability to physically configure the grating and the three spectral arms for particular wavelength combinations. Some combinations of wavelengths in the current filter set may not be possible, or they may suffer from reduced throughput, from vignetting or diffraction efficiency, or degraded image quality. The addition of a second grating with a different groove density would greatly improve the performance of the instrument for more spectral-line combinations. Although DL-NIRSP has fixed observing wavelengths limited by the availability of filters, the filter set can be extended. Community members interested in additional wavelengths and wavelength combinations are encouraged to contact the corresponding author.

Acknowledgments The research reported herein is based in part on data collected with the *Daniel K. Inouye Solar Telescope* (DKIST), a facility of the National Solar Observatory (NSO). NSO is managed by the Association of Universities for Research in Astronomy, Inc., and it is funded by the National Science Foundation. Any opinions, findings, and conclusions or recommendations expressed in this publication are those of the authors and do not necessarily reflect the views of the National Science Foundation or the Association of Universities for Research in Astronomy, Inc. DKIST is located on land of spiritual and cultural significance to Native Hawaiian people. The use of this important site to further scientific knowledge is done so with appreciation and respect.

The authors would like to thank supporting staff members at the University of Hawai'i Institute for Astronomy who assisted with this project, including Joey Perreira, Tom McCall, and Matt Maynard. The authors wish to thank the entire DKIST team, especially the construction and operations teams, and the following individuals: Friedrich Wöger, Thomas Rimmele, Stephanie Guzman, Shawn Culver, Heather Marshall, Paul Jeffers, and Lukas Rimmele for their support and assistance with the DL-NIRSP instrument project.

Author contributions Funding Acquisition: H. Lin; Instrument Design: P. Onaka, H. Lin, X.P. Huang, T. Schad, S. Jaeggli, H. McGregor, G. Nitta, M. Bonnet, L. Robertson, H. Yamada; Instrument Implementation: P. Onaka, S. Jaeggli, T. Anan, G. Ching, G. Nitta, L. Robertson, P. Toyama, J. Young, S. Sueoka, P. Sekulic, M. Liang, M. Puentes, D. Harrington, B. Smith, M. Kramar; Software: H. Yamada, C. Rae, C. Berst, T. Anan, M. Kramar, S. Jaeggli; Data Analysis: S. Jaeggli, T. Anan, T. Schad; Writing - original draft preparation: S. Jaeggli, H. Lin, T. Anan, T. Schad, P. Onaka, M. Kramar; Writing - review and editing: all authors.

Funding The research reported herein is based in part on data collected with the *Daniel K. Inouye Solar Telescope* (DKIST), a facility of the National Solar Observatory (NSO). NSO is managed by the Association of Universities for Research in Astronomy, Inc., and it is funded by the National Science Foundation. Open Access funding for this article has been provided by NSO.

Data Availability The data sets collected and analyzed during the course of this work were taken for engineering and performance verification and are not publicly available. Scientific data sets were taken before full commissioning of the instrument with the telescope and are not capable of being processed with the DKIST data-reduction pipeline, but may be made available on reasonable request to the corresponding author.

Code Availability The *DL-NIRSP Instrument Performance Calculator* is publicly available on the NSO website at nso.edu/telescopes/dkist/instruments/dl-nirsp/. The *DL-NIRSP Spectrograph Calculator* is available on request to the corresponding author.

Declarations

Disclosure of Potential Conflicts of Interest The authors declare that they have no conflicts of interest.

Competing interests The authors declare no competing interests.

Open Access This article is licensed under a Creative Commons Attribution 4.0 International License, which permits use, sharing, adaptation, distribution and reproduction in any medium or format, as long as you give appropriate credit to the original author(s) and the source, provide a link to the Creative Commons licence, and indicate if changes were made. The images or other third party material in this article are included in the article's Creative Commons licence, unless indicated otherwise in a credit line to the material. If material is not included in the article's Creative Commons licence and your intended use is not permitted by statutory regulation or exceeds the permitted use, you will need to obtain permission directly from the copyright holder. To view a copy of this licence, visit <http://creativecommons.org/licenses/by/4.0/>.

References

- Anan, T., Schad, T.A., Jaeggli, S.A., Tarr, L.A.: 2019, Shock heating energy of umbral flashes measured with integral field unit spectroscopy. *Astrophys. J.* **882**, 161. [DOI](#). [ADS](#).
- Anan, T., Schad, T.A., Kitai, R., Dima, G.I., Jaeggli, S.A., Tarr, L.A., Collados, M., Dominguez-Tagle, C., Kleint, L.: 2021, Measurements of photospheric and chromospheric magnetic field structures associated with chromospheric heating over a solar plage region. *Astrophys. J.* **921**, 39. [DOI](#). [ADS](#).
- Benz, A.O.: 2017, Flare observations. *Liv. Rev. Solar Phys.* **14**, 2. [DOI](#). [ADS](#).
- Borrero, J.M., Jafarzadeh, S., Schüssler, M., Solanki, S.K.: 2017, Solar magnetoconvection and small-scale dynamo. Recent developments in observation and simulation. *Space Sci. Rev.* **210**, 275. [DOI](#). [ADS](#).
- Cameron, R.H., Dikpati, M., Brandenburg, A.: 2017, The global solar dynamo. *Space Sci. Rev.* **210**, 367. [DOI](#). [ADS](#).
- Casini, R., de Wijn, A.G., Judge, P.G.: 2012, Analysis of seeing-induced polarization cross-talk and modulation scheme performance. *Astrophys. J.* **757**, 45. [DOI](#). [ADS](#).
- Casini, R., White, S.M., Judge, P.G.: 2017, Magnetic diagnostics of the solar corona: synthesizing optical and radio techniques. *Space Sci. Rev.* **210**, 145. [DOI](#). [ADS](#).
- Collados, M., López, R., Páez, E., Hernández, E., Reyes, M., Calcines, A., Ballesteros, E., Díaz, J.J., Denker, C., Lagg, A., Schlichenmaier, R., Schmidt, W., Solanki, S.K., Strassmeier, K.G., von der Lühe, O., Volkmer, R.: 2012, GRIS: the GREGOR infrared spectrograph. *Astron. Nachr.* **333**, 872. [DOI](#). [ADS](#).
- Cranmer, S.R., Winebarger, A.R.: 2019, The properties of the solar corona and its connection to the solar wind. *Annu. Astron. Astrophys.* **57**, 157. [DOI](#). [ADS](#).
- De Moortel, I., Browning, P.: 2015, Recent advances in coronal heating. *Phil. Trans. Roy. Soc. London Ser. A* **373**, 20140269. [DOI](#). [ADS](#).
- De Pontieu, B., Martínez-Sykora, J., Testa, P., Winebarger, A.R., Daw, A., Hansteen, V., Cheung, M.C.M., Antolin, P.: 2020, The multi-slit approach to coronal spectroscopy with the multi-slit solar explorer (MUSE). *Astrophys. J.* **888**, 3. [DOI](#). [ADS](#).
- de Wijn, A.G., Casini, R., Carlile, A., Lecinski, A.R., Sewell, S., Zmarzly, P., Eigenbrot, A.D., Beck, C., Wöger, F., Knölker, M.: 2022, The visible spectro-polarimeter of the Daniel K. Inouye Solar Telescope. *Solar Phys.* **297**, 22. [DOI](#). [ADS](#).
- del Toro Iniesta, J.C.: 2003, *Introduction to Spectropolarimetry*, Cambridge University Press, UK. [DOI](#).
- Del Zanna, G., Dere, K.P., Young, P.R., Landi, E.: 2021, CHIANTI—an atomic database for emission lines. XVI. Version 10, further extensions. *Astrophys. J.* **909**, 38. [DOI](#). [ADS](#).
- Dere, K.P., Landi, E., Mason, H.E., Monsignori Fossi, B.C., Young, P.R.: 1997, CHIANTI - an atomic database for emission lines. *Astron. Astrophys. Suppl.* **125**, 149. [DOI](#). [ADS](#).

- Dima, G.I., Kuhn, J.R., Schad, T.A.: 2019, Coronagraphic observations of Si X λ 14301 and Fe XIII λ 10747 linearly polarized spectra using the SOLARC telescope. *Astrophys. J.* **877**, 144. DOI. ADS.
- Dima, G.I., Schad, T.A.: 2020, Using multi-line spectropolarimetric observations of forbidden emission lines to measure single-point coronal magnetic fields. *Astrophys. J.* **889**, 109. DOI. ADS.
- Dominguez-Tagle, C., Collados, M., Lopez, R., Vaz Cedillo, J.J., Esteves, M.A., Grassin, O.: 2022, First light of the integral field unit of gris on the gregor solar telescope. *J. Astron. Instrum.* **11**, 2250014. DOI.
- Elmore, D.F., Lites, B.W., Tomczyk, S., Skumanich, A., Dunn, R.B., Schuenke, J.A., Streander, K.V., Leach, T.W., Chambellan, C.W., Hull, H.K., Lacey, L.B.: 1992, Advanced Stokes polarimeter: a new instrument for solar magnetic field research. In: Goldstein, D.H., Chipman, R.A. (eds.) *Polarization Analysis and Measurement, Soc. Photo-Opt. Instrum. Eng. (SPIE) CS-1746*, 22. DOI.
- Fehlmann, A.: 2022, The cryogenic near-infrared spectropolarimeter. *Solar Phys.*, in preparation.
- Felipe, T., Khomenko, E., Collados, M., Beck, C.: 2010, Multi-layer study of wave propagation in sunspots. *Astrophys. J.* **722**, 131. DOI. ADS.
- Ferayorni, A., Beard, A., Berst, C., Goodrich, B.: 2014, DKIST controls model for synchronization of instrument cameras, polarization modulators, and mechanisms. In: Chiozzi, G., Radziwill, N.M. (eds.) *Software and Cyberinfrastructure for Astronomy III, Soc. Photo-Opt. Instrum. Eng. (SPIE) CS-9152*, 91520Z. DOI. ADS.
- Fujimura, D., Tsuneta, S.: 2009, Properties of magnetohydrodynamic waves in the solar photosphere obtained with Hinode. *Astrophys. J.* **702**, 1443. DOI. ADS.
- Green, L.M., Török, T., Vršnak, B., Manchester, W., Veronig, A.: 2018, The origin, early evolution and predictability of solar eruptions. *Space Sci. Rev.* **214**, 46. DOI. ADS.
- Harrington, D.M., Sueoka, S.R.: 2018, Polarization modeling and predictions for DKIST part 3: focal ratio and thermal dependencies of spectral polarization fringes and optic retardance. *J. Astron. Telesc. Instrum. Syst.* **4**, 1. DOI.
- Harrington, D.M., Sueoka, S.R., White, A.J.: 2019, Polarization modeling and predictions for Daniel K. Inouye Solar Telescope part 5: impacts of enhanced mirror and dichroic coatings on system polarization calibration. *J. Astron. Telesc. Instrum. Syst.* **5**, 1. DOI.
- Harrington, D., Jaeggli, S.A., Schad, T.A., White, A.J., Sueoka, S.R.: 2020, Polarization modeling and predictions for Daniel K. Inouye Solar Telescope, part 6: fringe mitigation with polycarbonate modulators and optical contact calibration retarders. *J. Astron. Telesc. Instrum. Syst.* **6**, 1. DOI.
- Harrington, D.M., Wöger, F., White, A.J., Sueoka, S.R.: 2021, Polarization modeling and predictions for dkist, part 9: flux distribution with fido. *J. Astron. Telesc. Instrum. Syst.* **7**, 1. DOI.
- Harrington, D.M., Sueoka, S., Schad, T., Beck, C., Eigenbrot, A.D., de Wijn, A., Casini, R., White, A.J., Jaeggli, S.A.: 2022, Systems approach to polarization calibration for the Daniel K. Inouye Solar Telescope. *Solar Phys.*, submitted.
- Henault, F., Bacon, R., Bonneville, C., Boudon, D., Davies, R.L., Ferruit, P., Gilmore, G.F., Le Fèvre, O., Lemonnier, J.-P., Lilly, S., Morris, S.L., Prieto, E., Steinmetz, M., de Zeeuw, P.T.: 2003, MUSE: a second-generation integral-field spectrograph for the VLT. In: Iye, M., Moorwood, A.F.M. (eds.) *Instrument Design and Performance for Optical/Infrared Ground-Based Telescopes, Soc. Photo-Opt. Instrum. Eng. (SPIE) CS-4841*, 1096. DOI. ADS.
- Hubbard, J., Goodrich, B., Wampler, S.: 2010, The ATST base: command-action-response in action. In: Radziwill, N.M., Bridger, A. (eds.) *Software and Cyberinfrastructure for Astronomy, Soc. Photo-Opt. Instrum. Eng. (SPIE) CS-7740*, 77402R. DOI. ADS.
- Jaeggli, S.A., Lin, H., Mickey, D.L., Kuhn, J.R., Hegwer, S.L., Rimmele, T.R., Penn, M.J.: 2010, FIRS: a new instrument for photospheric and chromospheric studies at the DST. *Mem. Soc. Astron. Ital.* **81**, 763. ADS.
- Johansson, E.M., Goodrich, B.: 2012, Simultaneous control of multiple instruments at the advanced technology solar telescope. In: Radziwill, N.M., Chiozzi, G. (eds.) *Software and Cyberinfrastructure for Astronomy II, Soc. Photo-Opt. Instrum. Eng. (SPIE) CS-8451*, 84510J. DOI. ADS.
- Johnson, L.C., Cummings, K., Drobilek, M., Johansson, E., Marino, J., Rampy, R., Richards, K., Rimmele, T., Sekulic, P., Wöger, F.: 2018, Laboratory integration of the DKIST wavefront correction system. In: Close, L.M., Schreiber, L., Schmidt, D. (eds.) *Adaptive Optics Systems VI, Soc. Photo-Opt. Instrum. Eng. (SPIE) CS-10703*, 107030F. DOI. ADS.
- Kawabata, Y., Asensio Ramos, A., Inoue, S., Shimizu, T.: 2020, Chromospheric magnetic field: a comparison of He I 10830 Å observations with nonlinear force-free field extrapolation. *Astrophys. J.* **898**, 32. DOI. ADS.
- Klimchuk, J.A.: 2015, Key aspects of coronal heating. *Phil. Trans. Roy. Soc. London Ser. A* **373**, 20140256. DOI. ADS.
- Kramar, M., Inhester, B., Solanki, S.K.: 2006, Vector tomography for the coronal magnetic field. I. Longitudinal Zeeman effect measurements. *Astron. Astrophys.* **456**, 665. DOI. ADS.

- Kramar, M., Inhester, B., Lin, H., Davila, J.: 2013, Vector tomography for the coronal magnetic field. II. Hanle effect measurements. *Astrophys. J.* **775**, 25. DOI. ADS.
- Kurucz, R.L., Furenlid, I., Brault, J., Testerman, L.: 1984, Solar flux atlas from 296 to 1300 nm. *National Solar Observatory, Sunspot*. ADS.
- Lagg, A., Solanki, S.K., Riethmüller, T.L., Martínez Pillet, V., Schüssler, M., Hirzberger, J., Feller, A., Borrero, J.M., Schmidt, W., del Toro Iniesta, J.C., Bonet, J.A., Barthol, P., Berkefeld, T., Domingo, V., Gandorfer, A., Knölker, M., Title, A.M.: 2010, Fully resolved quiet-sun magnetic flux tube observed with the SUNRISE/IMAX instrument. *Astrophys. J. Lett.* **723**, L164. DOI. ADS.
- Landi, E., Habbal, S.R., Tomczyk, S.: 2016, Coronal plasma diagnostics from ground-based observations. *J. Geophys. Res.* **121**, 8237. DOI.
- Lemen, J.R., Title, A.M., Akin, D.J., Boerner, P.F., Chou, C., Drake, J.F., Duncan, D.W., Edwards, C.G., Friedlaender, F.M., Heyman, G.F., Hurlburt, N.E., Katz, N.L., Kushner, G.D., Levay, M., Lindgren, R.W., Mathur, D.P., McFeaters, E.L., Mitchell, S., Rehse, R.A., Schrijver, C.J., Springer, L.A., Stern, R.A., Tarbell, T.D., Wuelser, J.-P., Wolfson, C.J., Yanari, C., Bookbinder, J.A., Cheimets, P.N., Caldwell, D., Deluca, E.E., Gates, R., Golub, L., Park, S., Podgorski, W.A., Bush, R.I., Scherrer, P.H., Gummin, M.A., Smith, P., Auker, G., Jerram, P., Pool, P., Soufli, R., Windt, D.L., Beardsley, S., Clapp, M., Lang, J., Waltham, N.: 2012, The Atmospheric Imaging Assembly (AIA) on the Solar Dynamics Observatory (SDO). *Solar Phys.* **275**, 17. DOI. ADS.
- Lin, H.: 2012, SPIES: the spectropolarimetric imager for the energetic sun. In: McLean, I.S., Ramsay, S.K., Takami, H. (eds.) *Ground-Based and Airborne Instrumentation for Astronomy IV, Soc. Photo-Opt. Instrum. Eng. (SPIE) CS-8446*, 84461D. DOI.
- Lin, H.: 2016, mxCSM: a 100-slit, 6-wavelength wide-field coronal spectropolarimeter for the study of the dynamics and the magnetic fields of the solar corona. *Front. Astron. Space Sci.* **3**, 9. DOI. ADS.
- Lin, H., Kuhn, J.R., Coulter, R.: 2004, Coronal magnetic field measurements. *Astrophys. J. Lett.* **613**, L177. DOI. ADS.
- Lin, H., Penn, M.J., Tomczyk, S.: 2000, A new precise measurement of the coronal magnetic field strength. *Astrophys. J. Lett.* **541**, L83. DOI. ADS.
- Lin, H., Versteegh, A.: 2006, VisIRIS: a visible/IR imaging spectropolarimeter based on a birefringent fiber-optic image slicer. In: McLean, I.S., Iye, M. (eds.) *Ground-Based and Airborne Instrumentation for Astronomy, Soc. Photo-Opt. Instrum. Eng. (SPIE) CS-6269*, 62690K. DOI.
- Lites, B.W.: 1987, Rotating waveplates as polarization modulators for Stokes polarimetry of the sun: evaluation of seeing-induced crosstalk errors. *Appl. Opt.* **26**, 3838. DOI. ADS.
- Martin, S.F., Ramsey, H.E., Carroll, G.A., Martin, D.C.: 1974, A multi-slit spectrograph and H α Doppler system. *Solar Phys.* **37**, 343. DOI. ADS.
- Metcalf, T.R., Jiao, L., McClymont, A.N., Canfield, R.C., Uitenbroek, H.: 1995, Is the solar chromospheric magnetic field force-free? *Astrophys. J.* **439**, 474. DOI. ADS.
- Morosin, R., de la Cruz Rodríguez, J., Vissers, G.J.M., Yadav, R.: 2020, Stratification of canopy magnetic fields in a plage region. Constraints from a spatially-regularized weak-field approximation method. *Astron. Astrophys.* **642**, A210. DOI. ADS.
- Okamoto, K.: 2006, Chapter 3 - optical fibers. In: Okamoto, K. (ed.) *Fundamentals of Optical Waveguides*, 2nd edn., Academic Press, Burlington, 57. 978-0-12-525096-2. DOI.
- Onaka, P., Tonry, J.L., Isani, S., Lee, A., Uyeshiro, R., Rae, C., Robertson, L., Ching, G.: 2008, The pan-STARRS gigapixel camera #1 and STARGRASP controller results and performance. In: McLean, I.S., Casali, M.M. (eds.) *Ground-Based and Airborne Instrumentation for Astronomy II, Soc. Photo-Opt. Instrum. Eng. (SPIE) CS-7014*, 178. DOI.
- Palmer, C.: 2020, *The Diffraction Grating Handbook*, 8th edn. MKS Instruments, Rochester.
- Penn, M.J., Kuhn, J.R.: 1994, How bright is the [Si X] 1431 nm coronal emission line? *Solar Phys.* **151**, 51. DOI. ADS.
- Pesnell, W.D., Thompson, B.J., Chamberlin, P.C.: 2012, The Solar Dynamics Observatory (SDO). *Solar Phys.* **275**, 3. DOI. ADS.
- Quintero Noda, C., Kato, Y., Katsukawa, Y., Oba, T., de la Cruz Rodríguez, J., Carlsson, M., Shimizu, T., Orozco Suárez, D., Ruiz Cobo, B., Kubo, M., Anan, T., Ichimoto, K., Suematsu, Y.: 2017, Chromospheric polarimetry through multiline observations of the 850-nm spectral region - II. A magnetic flux tube scenario. *Mon. Not. Roy. Astron. Soc.* **472**, 727. DOI. ADS.
- Ramsay Howat, S.K., Todd, S., Leggett, S., Davis, C., Strachan, M., Borrowman, A., Ellis, M., Elliot, J., Gostick, D., Kackley, R., Rippla, M.: 2004, The commissioning of and first results from the UIST imager spectrometer. In: Moorwood, A.F.M., Iye, M. (eds.) *Ground-Based Instrumentation for Astronomy, Soc. Photo-Opt. Instrum. Eng. (SPIE) CS-5492*, 1160. DOI. ADS.
- Rast, M.P., Bello González, N., Bellot Rubio, L., Cao, W., Cauzzi, G., Deluca, E., de Pontieu, B., Fletcher, L., Gibson, S.E., Judge, P.G., Katsukawa, Y., Kazachenko, M.D., Khomenko, E., Landi, E., Martínez Pillet, V., Petrie, G.J.D., Qiu, J., Rachmeler, L.A., Rempel, M., Schmidt, W., Scullion, E., Sun, X.,

- Welsch, B.T., Andretta, V., Antolin, P., Ayres, T.R., Balasubramaniam, K.S., Ballai, I., Berger, T.E., Bradshaw, S.J., Campbell, R.J., Carlsson, M., Casini, R., Centeno, R., Cramer, S.R., Criscuolo, S., Deforest, C., Deng, Y., Erdélyi, R., Fedun, V., Fischer, C.E., González Manrique, S.J., Hahn, M., Harra, L., Henriques, V.M.J., Hurlburt, N.E., Jaeggli, S., Jafarzadeh, S., Jain, R., Jefferies, S.M., Keys, P.H., Kowalski, A.F., Kuckein, C., Kuhn, J.R., Kuridze, D., Liu, J., Liu, W., Longcope, D., Mathioudakis, M., McAteer, R.T.J., McIntosh, S.W., McKenzie, D.E., Miralles, M.P., Morton, R.J., Muglach, K., Nelson, C.J., Panesar, N.K., Parenti, S., Parnell, C.E., Poduval, B., Reardon, K.P., Reep, J.W., Schad, T.A., Schmit, D., Sharma, R., Socas-Navarro, H., Srivastava, A.K., Sterling, A.C., Suematsu, Y., Tarr, L.A., Tiwari, S., Tritschler, A., Verth, G., Vourlidas, A., Wang, H., Wang, Y.-M.: 2021, Critical science plan for the Daniel K. Inouye Solar Telescope (DKIST). *Solar Phys.* **296**, 70. DOI ADS.
- Rempel, M.: 2014, Numerical simulations of quiet sun magnetism: on the contribution from a small-scale dynamo. *Astrophys. J.* **789**, 132. DOI ADS.
- Ren, D., Keller, C., Plymate, C.: 2009, An IFU for diffraction-limited 3D spectroscopic imaging: laboratory and on-site tests. In: Fineschi, S., Fennelly, J.A. (eds.) *Solar Physics and Space Weather Instrumentation III, Soc. Photo-Opt. Instrum. Eng. (SPIE) CS-7438*, 743818. DOI ADS.
- Richards, K., Rimmele, T., Hegwer, S.L., Upton, R.S., Woeger, F., Marino, J., Gregory, S., Goodrich, B.: 2010, The adaptive optics and wavefront correction systems for the advanced technology solar telescope. In: Ellerbroek, B.L., Hart, M., Hubin, N., Wizinowich, P.L. (eds.) *Adaptive Optics Systems II, Soc. Photo-Opt. Instrum. Eng. (SPIE) CS-7736*, 773608. DOI ADS.
- Rimmele, T., Richards, K., Roche, J.M., Hegwer, S.L., Hubbard, R.P., Hansen, E.R., Goodrich, B., Upton, R.S.: 2006, The wavefront correction system for the advanced technology solar telescope. In: Ellerbroek, B.L., Calia, D.B. (eds.) *Advances in Adaptive Optics II, Soc. Photo-Opt. Instrum. Eng. (SPIE) CS-6272*, 627212. DOI.
- Rimmele, T.R., Warner, M., Keil, S.L., Goode, P.R., Knölker, M., Kuhn, J.R., Rosner, R.R., McMullin, J.P., Casini, R., Lin, H., Wöger, F., von der Lühe, O., Tritschler, A., Davey, A., de Wijn, A., Elmore, D.F., Fehlmann, A., Harrington, D.M., Jaeggli, S.A., Rast, M.P., Schad, T.A., Schmidt, W., Mathioudakis, M., Mickey, D.L., Anan, T., Beck, C., Marshall, H.K., Jeffers, P.F., Oschmann, J.M., Beard, A., Berst, D.C., Cowan, B.A., Craig, S.C., Cross, E., Cummings, B.K., Donnelly, C., de Vanssay, J.-B., Eigenbrot, A.D., Ferayorni, A., Foster, C., Galapon, C.A., Gedrites, C., Gonzales, K., Goodrich, B.D., Gregory, B.S., Guzman, S.S., Guzzo, S., Hegwer, S., Hubbard, R.P., Hubbard, J.R., Johansson, E.M., Johnson, L.C., Liang, C., Liang, M., McQuillen, I., Mayer, C., Newman, K., Onodera, B., Phelps, L., Puentes, M.M., Richards, C., Rimmele, L.M., Sekulic, P., Shimko, S.R., Simison, B.E., Smith, B., Starman, E., Sueoka, S.R., Summers, R.T., Szabo, A., Szabo, L., Wampler, S.B., Williams, T.R., White, C. (eds.): 2020, The Daniel K. Inouye Solar Telescope - observatory overview. *Solar Phys.* **295**, 172. DOI ADS.
- Schad, T., Dima, G.: 2020, Forward synthesis of polarized emission in target DKIST coronal lines applied to 3D MURaM coronal simulations. *Solar Phys.* **295**, 98. DOI ADS.
- Schad, T., Lin, H.: 2017, Infrared imaging spectroscopy using massively multiplexed slit-based techniques and sub-field motion correction. *Solar Phys.* **292**, 158. DOI ADS.
- Schad, T., Lin, H., Ichimoto, K., Katsukawa, Y.: 2014, Polarization properties of a birefringent fiber optic image slicer for diffraction-limited dual-beam spectropolarimetry. In: Ramsay, S.K., McLean, I.S., Takami, H. (eds.) *Ground-Based and Airborne Instrumentation for Astronomy V, Soc. Photo-Opt. Instrum. Eng. (SPIE) CS-9147*, 91476E. DOI ADS.
- Schou, J., Scherrer, P.H., Bush, R.I., Wachter, R., Couvidat, S., Rabello-Soares, M.C., Bogart, R.S., Hoeksema, J.T., Liu, Y., Duvall, T.L., Akin, D.J., Allard, B.A., Miles, J.W., Rairden, R., Shine, R.A., Tarbell, T.D., Title, A.M., Wolfson, C.J., Elmore, D.F., Norton, A.A., Tomczyk, S.: 2012, Design and ground calibration of the Helioseismic and Magnetic Imager (HMI) instrument on the Solar Dynamics Observatory (SDO). *Solar Phys.* **275**, 229. DOI ADS.
- Snee, S.A., Gunn, J.E., Uomoto, A., Roe, N., Schlegel, D., Rockosi, C.M., Carr, M.A., Leger, F., Dawson, K.S., Olmstead, M.D., Brinkmann, J., Owen, R., Barkhouser, R.H., Honscheid, K., Harding, P., Long, D., Lupton, R.H., Loomis, C., Anderson, L., Annis, J., Bernardi, M., Bhardwaj, V., Bizyaev, D., Bolton, A.S., Brewington, H., Briggs, J.W., Burles, S., Burns, J.G., Castander, F.J., Connolly, A., Davenport, J.R.A., Ebelke, G., Epps, H., Feldman, P.D., Friedman, S.D., Frieman, J., Heckman, T., Hull, C.L., Knapp, G.R., Lawrence, D.M., Loveday, J., Mannery, E.J., Malanushenko, E., Malanushenko, V., Merrelli, A.J., Muna, D., Newman, P.R., Nichol, R.C., Oravetz, D., Pan, K., Pope, A.C., Ricketts, P.G., Shelden, A., Sandford, D., Siegmund, W., Simmons, A., Smith, D.S., Snedden, S., Schneider, D.P., SubbaRao, M., Tremonti, C., Waddell, P. York, D.G.: 2013, The multi-object, fiber-fed spectrographs for the sloan digital sky survey and the baryon oscillation spectroscopic survey. *Astrophys. J.* **146**, 32. DOI ADS.
- Terrien, R.C., Monson, A.J., Mahadevan, S., Bender, C., Halverson, S.P., Ramsey, L.: 2016, Measuring extended red sensitivity in a 1.7 micron-cutoff HgCdTe detector array. In: Holland, A.D., Beletic, J. (eds.)

High Energy, Optical, and Infrared Detectors for Astronomy VII, Soc. Photo-Opt. Instrum. Eng. (SPIE) CS-9915, 595. DOI.

- Versteegh, A.: 2006, Image reconstruction for a fiber-fed integral field spectropolarimeter. Master's thesis, Technische Universiteit Eindhoven.
- von der Lühe, O., et al.: 2022, The Daniel K. Inouye Solar Telescope (DKIST)/Visible Tunable Filter. *Solar Phys.*, in preparation.
- Wöger, F., Rimmele, T., Ferayorni, A., Beard, A., Gregory, B.S., Sekulic, P., Hegwer, S.L.: 2021, The Daniel K. Inouye Solar Telescope (DKIST)/Visible Broadband Imager (VBI). *Solar Phys.* **296**, 145. DOI. ADS.

Publisher's Note Springer Nature remains neutral with regard to jurisdictional claims in published maps and institutional affiliations.

Authors and Affiliations

Sarah A. Jaeggli¹  · Haosheng Lin²  · Peter Onaka³ · Hubert Yamada³ · Tetsu Anan¹  · Morgan Bonnet³ · Gregory Ching³ · Xiao-Pei Huang⁴ · Maxim Kramar² · Helen McGregor⁵ · Garry Nitta² · Craig Rae³ · Louis Robertson³ · Thomas A. Schad¹  · Paul Toyama³ · Jessica Young³ · Chris Berst⁶ · David M. Harrington¹  · Mary Liang¹ · Myles Puentes⁵ · Predrag Sekulic⁷ · Brett Smith⁸ · Stacey R. Sueoka¹

✉ S.A. Jaeggli
sjaeggli@nso.edu

H. Lin
haosheng@hawaii.edu

- ¹ National Solar Observatory, 22 Ohia Ku Street, Pukalani, HI 96768, USA
- ² Institute for Astronomy, University of Hawai'i, 24 Ohia Ku Street, Pukalani, HI 96768, USA
- ³ Institute for Astronomy, University of Hawai'i, 2680 Woodlawn Drive, Honolulu, HI 96822, USA
- ⁴ Ball Aerospace, 1600 Commerce Street, Boulder, CO 80301, USA
- ⁵ Australian Astronomical Optics, 105 Delhi Road, North Ryde, NSW 2113, Australia
- ⁶ National Solar Observatory, 3665 Discovery Drive, Boulder, CO 80303, USA
- ⁷ KBR/NASA Goddard Space Flight Center, 8800 Greenbelt Road, Greenbelt, MD 20771, USA
- ⁸ W.M. Keck Observatory, 65-1120 Mamalahoa Highway, Kamuela, HI 96743, USA